NUMERICAL STUDY OF PARTICLE BED SCOUR BY VORTICES

A Thesis Presented

by

Dan Hagan

to

The Faculty of the Graduate College

of

The University of Vermont

In Partial Fullfillment of the Requirements
for the Degree of Master of Science
Specializing in Mechanical Engineering

October, 2014

Accepted by the Faculty of the Graduate College, The University of Vermont, in partial fulfillment of the requirements for the degree of Master of Science, specializing in Mechanical Engineering.

Thesis Examination Committee:

_____ Advisor
Yves Dubief, Ph.D.

_____ Advisor
Mandar Dewoolkar, Ph.D.

_____
Darren Hitt, Ph.D.

_____ Chairperson
George Pinder, Ph.D.

_____ Dean, Graduate College
Cynthia J. Forehand, Ph.D.

Date: July 2, 2014

Abstract

Scouring is the process of soil or sediment erosion due to flowing water, which can lead to bed degradation and compromised transportation infrastructure. In the decade before 2000, over half of the 500 bridge failures in the United States were caused by flooding or scouring. To gain a better grasp of the effects of extreme weather events, such as Tropical Storm Irene, on the scouring process, this work is focused on a first principle understanding of the mechanism(s) of scour. The field of Computational Fluid Dynamics (CFD) is particularly well suited to this task. Utilizing a Direct Numerical Simulation (DNS) code, the repeated impacts of a vortex dipole on a particle bed are simulated. The resulting scour characteristics and flow dynamics are investigated as a function of the Shields number. The vortex dipole propagates perpendicularly to the particle bed, resulting in the scouring of the bed and dissipation of the dipole. After completion of the scour event, the simulation is repeated four more times, where subsequent simulations use the scoured bed from the previous simulation as the initial bed form. This simulation series is conducted over a Shields number parameter space. The fluid phase is treated as a continuum and the discretized Navier-Stokes equations are solved down to the smallest scales of the flow on an Eulerian grid. The particles comprising the bed are represented by the Discrete Particle Model (DPM), whereby each individual particle is tracked in a Lagrangian framework. Particle-particle and particle-wall collisions are calculated using a soft-sphere model. The fluid phase and the solid phase are coupled through a forcing term in the fluid conservation of momentum equation, and a drag force in the particle equation of motion, governed by Newton's Second Law. Above the critical Shields number, the scour hole topography is not fundamentally altered with subsequent impacts until the scale of the scour hole reaches a critical value. At which point, the shape and scale of the scour hole significantly alters the behavior of the vortex dipole and results in strongly asymmetric scour topographies. This two-way coupling between the bed scour and the vortex dipole dynamics is the focus of this work.

Table of Contents

List of Figures

List of Tables

Chapter 1

Introduction and Literature Review

Between 1989 and 2000, over 500 bridges failed in the United States, with 53% of the failures caused by flooding or scouring (Wardhana and Hadipriono 2003). The Federal Highway Administration defines scour as "erosion or removal of streamed or bank material from bridge foundations due to flowing water, usually considered as long-term bed degradation [or] contraction." Accordingly, the federal aid system spends $50 million annually on highway flood damage (Lagasse et al. 1995). Additionally, the Intergovernmental Panel on Climate Change (IPCC) concluded that the Earth is becoming warmer in their 2007 report (IPCC 2007). The mean global temperature has increased roughly $1.5°$F since 1900, and is projected to rise anywhere from $2°$F to $11.5°$F by 2100 (USGCRP 2009). While the regional effects will vary, predictions for the state of Vermont, in the North Eastern United States, project increased heavy precipitation, warmer winters resulting in more precipitation in the form of rain rather than snow, and earlier spring snowmelts (Betts 2011). As a result, regions like Vermont can expect increased stress on transportation infrastructure like roads and bridges in particular, due to the increased intensity and frequency of river and runoff flow. In 2011, Tropical Storm Irene devastated many parts of the North Eastern seaboard, and Vermont sustained substantial damage, see Figure 1.1. Over 500 miles of roadway, over 2000 road segments, roughly 480 bridges, and almost 1000 culverts were damaged due to flooding from this extreme weather event. In addition to the immeasurable human toll, Irene inflicted hundreds of millions of dollars of repair costs (Pealer 2012).

(a) Scour behind a bridge abutment in Ludlow, VT   (b) VT Route 107

Figure 1.1: Examples of the effects of scour and erosion on transportation infrastructure, from Tropical Storm Irene.

1.1 Introduction

A significant amount of research effort has been dedicated to understanding scour processes, so a wealth of knowledge has been accrued in the literature and books. As noted by in the review of mathematical scour models by Sumer (Mutlu Sumer 2007), the following books are good resources: Breusers and Raudkivi (Breusers and Raudkivi 1991) cover scouring by rivers and streams around hydraulic structures; Hoffmans and Verheij (Hoffmans and Verheij 1997) wrote extensively about the scour process and associated models; Hoffmans also wrote about the influence of turbulence on soil erosion (Hoffmans 2012); and, Melville and Coleman (Melville and Coleman 2000) wrote specifically about bridge scour.

1.1.1 Literature Review

Numerous experimental setups have been used to study the scour phenomena. However, only a handful of canonical experimental setups will be mentioned here, particularly those that lend themselves well to numerical simulations. The first is erosion by a wall jet parallel to the surface of a sediment bed. Hassan and Narayanan (Nik Hassan and Narayanan 1985) measured the scour rate due to a wall jet issuing through a sluice opening beneath a rigid apron (non-erodable surface) for a range of sediment sizes, sluice openings, jet velocities, and apron lengths. Chatterjee et al. (Chatterjee et al. 1994) developed empirical relationships for the temporal characteristics of the scour depth and downstream sediment accretion peak of a sluice gate jet flowing over an apron then over an erodible sediment bed. Uyumaz (Uyumaz 1988) investigated the scour

2

phenomenon of flow passing below and over a sluice gate. Hamidifar et al. (Hamidifar et al. 2011) conducted a parametric study of scour hole depth and location for a range of apron roughnesses and submergence depths. Hopfinger et al. (Hopfinger et al. 2004) cited Gortler vortices, which form due to the concave shape of the eroded sediment bed, as the cause of turbulent boundary layer destabilization at the sediment bed. Bove et al. (Bove et al. 2013) observed new regimes in which two holes in the streamwise direction are generated by scouring processes.

The study of flow past abutments, like a vertical pier or over a petroleum pipeline lying horizontally on a soil bed, have also yielded insights into the nature of scour processes. Barbhuiya and Dey (Barbhuiya and Dey 2004) provide a review of local scour at common bridge abutments, highlighting the nature of the flow field, the accompanying shear stress, and resulting scour, as a function of approaching flow, abutment and bed sediment parameters.

Vortex rings have received much research attention. Von Helmholz (von Helmholtz 1867) applied a rigorous mathematical analysis to vortex rings that has paved the way for a large body of work analyzing many aspects of vortex ring motion and interactions. A review of vortex-wall interactions is given by Doligalski et al. (Doligalski et al. 1994). But, despite the fundamental nature of the vortex ring, it has been used sparingly in the study of sediment erosion. Sano et al. (Sano et al. 2008) and Munro et al. (Munro et al. 2009) have conducted experiments in which a vortex dipole collides with a erodible sediment bed. Munro measured the deformation of the sediment bed for a range of vortex ring impulse strengths, and sediment particle sizes and densities. Using a variety of vortex ring strengths and initial distances from the particle bed, Masuda et al. (Masuda et al. 2012) and Yoshida (Yoshida et al. 2012) explained the scour pattern regimes associated with particular Reynolds number ranges and initial distances.

With advancements in computing capabilities and algorithm efficiency, numerical simulations have become a viable alternative to experimental research. Unlike an experiment, which requires probes and/or imaging capabilities to capture data from the system, Computational Fluid Dynamics (CFD) have the advantage of access to data at any time or place in the simulation. Numerical simulations also allow parametric studies. CFD has its own limitations, e.g. boundary conditions, limited domain size. Yet CFD, with its access to full 4D information, enables detailed investigation into the physics at play and can be used as a complement to experiment, providing access to information beyond the reach of experimental methods.

Numerical studies of scour have traditionally treated the sediment bed as a continuum, so the bed load, and if represented, the suspended load, are treated as scalar concentrations. The morphology of the sediment bed is governed by a bed load transport equation and the suspended load is governed by the convection-diffusion transport equation. The majority of the work that uses this bed load approach use either Reynolds Averaged Navier-Stokes (RANS) simulations or Large Eddy Simulation (LES) to model flow. Both numerical methods are covered extensively in the literature, so a detailed review will not be given here. However, it is important to note that these methods model all (RANS) or small-scale (LES) flow structures, and must rely on turbulence models for non-laminar flows. By design, RANS solvers use time-averaged equations. Flow variables are decomposed into two components, the time-averaged value, and the fluctuation. Therefore, RANS solvers cannot accurately predict strongly time-dependent phenomena, like sediment scour. LES essentially applies the flow variables through a low-pass filter, removing the small-scale structures. The large scales of the flow are fully resolved directly, but the small scales are modeled in order to reduce computational cost. Since sediment scour occurs at the interface between the fluid and the sediment bed, exactly where the smallest scales of the flow are generated, LES may be filtering out flow characteristics that are crucial to scouring processes.

Mutlu Sumer (Mutlu Sumer 2007) provides a good general review of mathematical and numerical scour modeling. Tao and Yu (Tao and Yu 2013) have also compiled a thorough and clear review of these methods; a synopsis of this portion of their review follows. Although there are many variations of the bed load transport equation and approaches to couple the flow to the sediment phase, they are fundamentally similar in that they do not model the individual sediment particles. The heart of this method is based on the relationship between the sediment bed height and the rate of sediment flux. Paola and Voller (Paola and Voller 2005) derived a generalized Exner equation for the mass balance of sediment:

$$\frac{\partial h}{\partial t} = -\frac{1}{1-\lambda} \left(\nabla \cdot \mathbf{q} \right) \tag{1.1}$$

Where h is height of the sediment bed, λ is the porosity of the sediment bed, and $\mathbf{q}$ is the sediment flux vector (containing both bed load and suspended load fluxes). See Tao and Yu (Tao and Yu 2013) for the various forms the Exner equation can take. To determine the change to the sediment bed height, the flux $\mathbf{q}$ must be determined. The sediment flux vector $\mathbf{q}$ is a function of bed shear stress and the characteristics of

the sediment (diameter, density, etc.), for which there are a variety of empirical formulas. Tao and Yu (Tao and Yu 2013) selected three such commonly used formulas, one of which is reproduced here. The Van Rijn equation (Van Rijn 1984) assumes a constant τ_b^*,

$$\mathbf{q}_b^* = \frac{0.053}{d^{*0.3}} 8 \left(\frac{\tau_b - \tau_b^*}{\tau_b^*} \right) \tag{1.2}$$

For any formulation of $\mathbf{q}_b^*$, the direction of the flux is determined by the critical bed shear stress, τ_b^*, above which incipient sediment particle motion is observed. For a given sediment, the critical Shields stress number

$$\Theta^* = \frac{\tau_b^*}{(s-1)\rho_p g d^3} \tag{1.3}$$

defines this threshold. $\tau_b^* = \rho \mathbf{u}_f^2$ is the critical bed shear stress, $\mathbf{u}_f$ is the shear velocity, s is the specific density of a sediment particle, ρ_p is the density of a sediment particle, d is the diameter, and g is gravity. If $\Theta > \Theta^*$ then there is motion of the sediment particles. Incipient motion can also be determined by use of critical velocity at or near the wall, rather than the critical bed shear stress. If the effects of the suspended load are not to be ignored, then any entrained sediment is governed by the transport equation:

$$\frac{\partial c}{\partial t} + \nabla \cdot (c\mathbf{u}) = \nabla \cdot (D\nabla c) \tag{1.4}$$

Where c is the suspended load concentration and D is the diffusivity.

Since the individual sediment particles themselves are not modeled, various physical effects of the bed morphology and flow structures are accounted for with correction factors. When the slope of the bed morphology takes on an angle greater than the angle of repose for the sediment, τ_b^* is multiplied by a slope correction factor to model the potential sliding of individual sediment particles and the increased exposure to the effects of the fluid. For highly turbulent flows, the effects of turbulence and lift forces are significant and must be addressed with additional correction factors, in the same form as that for slope correction. Thus, to include the effects of bed slope angle, turbulence, and lift forces, the modified critical bed shear stress becomes

$$\tau_{b,modified}^* = (r_{slope} \cdot r_{turbulence} \cdot r_{lift}) \cdot \tau_b^* \tag{1.5}$$

Coupling the governing equations of the sediment to the flow has been done a couple of ways. But, the most commonly used method loosely couples the sediment bed load, suspended load, and bed morphology to the flow solver using the following algorithm (Tao and Yu 2013), whereby: (1) the flow field is solved with current bed morphology; (2) the change to the bed morphology is calculated with the Exner equation; (3) the flow-bed interface boundary is updated accordingly; (4) the flow field is solved for the new bed morphology. The algorithm is repeated until the bed morphology has reached a steady state.

The various forms of the bed load methodology has been used extensively in the literature. Olsen and Melaaen (Olsen and Melaaen 1993), Olsen and Kjellesvig (Olsen and Kjellesvig 1998), Roulund et al. (Roulund et al. 2005), and Liu and Garcia (Liu and García 2008) have simulated vertical circular piles using this technique. Olsen and Melaaen (Olsen and Melaaen 1993) and Olsen and Kjellesvig (Olsen and Kjellesvig 1998) used RANS flow solvers with a $k - \epsilon$ turbulence model, and Van Rijn's bed load concentration formulation (van Rijn 1987) in concert with the convection-diffusion transport equation for sediment concentration. Roulund et al. (Roulund et al. 2005) used a RANS flow solver with a $k - \omega$ turbulence model, and the bed load rate of Engelund and Fredsoe (Frank and Jørgen 1976). Liu and Garcia (Liu and García 2008) simulated 3D flow around a circular pile and 2D wall jet scour. They utilized a RANS flow solver with a $k - \epsilon$ turbulence model and the bed load rate of Engelund and Fredsoe (Frank and Jørgen 1976). Brørs (Brørs 1999), Li and Cheng (Li and Cheng 1999), and Liang et al. (Liang et al. 2005) have used the bed load methodology to simulate the flow and scour below a pipeline, which is represented by a cylinder lying on an erodible sediment bed axially perpendicular to the flow. Brørs (Brørs 1999) used a RANS flow solver with a $k - \epsilon$ turbulence model and a bed load transport rate for a horizontal bed with a slope correction factor. Li and Cheng (Li and Cheng 1999) use a potential flow model and an iterative process to model transient height of the sediment bed using a critical velocity methodology. Liang et al. (Liang et al. 2005) compare the results of a RANS solver with a $k - \epsilon$ closure model against a spatially filtered Navier-Stokes solver with a sub-grid scale (SGS) model. Both solvers are coupled with the bed load rate model of Van Rijn (van Rijn 1987). Hogg et al. (Hogg et al. 1997) simulated a 2D turbulent wall jet over an erodible boundary using a RANS solver and the bed load transport rate of Meyer-Peter and Muller (Meyer-Peter and Müller 1948). Chou and Fringer (Chou and Fringer 2010) used LES and the bed load transport rate of Meyer-Peter and Muller (Meyer-Peter and Müller 1948) to simulate a 3D turbulent boundary layer over an erodible surface.

CHAPTER 1. INTRODUCTION AND LITERATURE REVIEW

An alternative numerical approach to the bed load transport method is the Discrete Particle Model (DPM), which is used in this work. The DPM treats the fluid as a continuum and the particles as distinct entities. The model is two-way coupled, whereby the fluid feels the effects of each particle, and each particle feels the effect of the the surrounding fluid. The model was pioneered by Cundall and Strack (Cundall and Strack 1979). The details of the model are illustrated in Section 2.2, following the application by Pepiot and Desjardins (Pepiot and Desjardins 2012). Zhu et al. (Zhu et al. 2007, Zhu et al. 2008) review the theoretical developments of the method and provide a summary of DPM applications and findings. The DPM has many applications, including fluidized beds (see the review of DPM application to fluidized beds by Deen et al. (Deen et al. 2007)) and other particle-fluid flows. However, there has been limited application to the study of scour. Zamankhan (Zamankhan 2009) used LES and DPM to simulate 3D flow over a pipeline, and found good agreement with experimental results.

Chapter 2

Journal of Turbulence: Numerical study of particle bed scour by vortices

The repeated impacts of a vortex dipole on a particle bed are simulated using a Direct Numerical Simulation (DNS) code. The resulting scour characteristics and flow dynamics are investigated as a function of the Shields number. The vortex dipole propagates perpendicularly to the particle bed, resulting in the scouring of the bed and dissipation of the dipole. After completion of the scour event, the simulation is repeated four more times, where subsequent simulations use the scoured bed from the previous simulation as the initial bed form. This simulation series is conducted over a Shields number parameter space. The fluid phase is treated as a continuum and the discretized Navier-Stokes equations are solved down to the smallest scales of the flow, on an Eulerian grid. The particles comprising the bed are represented by the Discrete Particle Model (DPM), whereby each individual particle is tracked in a Lagrangian framework. Particle-particle and particle-wall collisions are modeled using a soft-sphere model. The fluid phase and the solid phase are coupled through a forcing term in the fluid conservation of momentum equation, and a drag force in the particle equation of motion, governed by Newton's Second Law. Above the critical Shields number, the scour hole topography is not fundamentally altered with subsequent impacts until the scale of the scour hole reaches a critical value. At which point, the shape and scale of the scour hole significantly alters the behavior of the vortex dipole and results in

8

strongly asymmetric scour topographies. The two-way coupling between the bed scour and the vortex dipole dynamics are analyzed.

2.1 Introduction

A significant amount of research effort has been dedicated to understanding scour processes, so a wealth of knowledge has been accrued in the literature and books. As noted by in the review of mathematical scour models by Mutlu Sumer (Mutlu Sumer 2007), the following books are good resources: Breusers and Raudkivi (Breusers and Raudkivi 1991) cover scouring by rivers and streams around hydraulic structures; Hoffmans and Verheij (Hoffmans and Verheij 1997) wrote extensively about the scour process and associated models; Hoffmans (Hoffmans 2012) also wrote about the influence of turbulence on soil erosion; and, Melville and Coleman (Melville and Coleman 2000) wrote specifically about bridge scour.

Numerous experimental setups have been used to study the scour phenomena. However, only a handful of canonical experimental setups will be mentioned here, particularly those that lend themselves well to numerical simulations. The first is erosion by a wall jet parallel to the surface of a sediment bed. Hassan and Narayanan (Nik Hassan and Narayanan 1985) measured the scour rate due to a wall jet issuing through a sluice opening beneath a rigid apron (non-erodable surface) for a range of sediment sizes, sluice openings, jet velocities, and apron lengths. Chatterjee et al. (Chatterjee et al. 1994) developed empirical relationships for the temporal characteristics of the scour depth and downstream sediment accretion peak of a sluice gate jet flowing over an apron then over an erodible sediment bed. Uyumaz (Uyumaz 1988) investigated the scour phenomenon of flow passing below and over a sluice gate. Hamidifar et al. (Hamidifar et al. 2011) conducted a parametric study of scour hole depth and location for a range of apron roughnesses and submergence depths. Hopfinger et al. (Hopfinger et al. 2004) cited Gortler vortices, which form due to the concave shape of the eroded sediment bed, as the cause of turbulent boundary layer destabilization at the sediment bed. Bove et al. (Bove et al. 2013) observed new regimes in which two holes in the streamwise direction are generated by scouring processes.

The study of flow past abutments, vertical piers or over a petroleum pipelines lying horizontally on a soil bed, have also yielded insights into the nature of scour processes. Barbhuiya and Dey (Barbhuiya and Dey 2004) provide a review of local scour at common bridge abutments, highlighting the nature of the flow

field, the accompanying shear stress, and resulting scour, as a function of approaching flow, abutment and bed sediment parameters.

Vortex rings have received quite a bit of attention in past research, but they have seen limited use in the study of erosion. Von Helmholz (von Helmholtz 1867) applied a rigorous mathematical analysis to vortex rings that has paved the way for a large body of work analyzing many aspects of vortex ring motion and interactions. A review of vortex-wall interactions is given by Doligalski et al. (Doligalski et al. 1994). Sano et al. (Sano et al. 2008) and Munro (Munro et al. 2009) have conducted experiments in which a vortex dipole collides with a erodible sediment bed. Munro (Munro et al. 2009) measured the deformation of the sediment bed for a range of vortex ring impulse strengths, and sediment particle sizes and densities. Using a variety of vortex ring strengths and initial distances from the particle bed, Masuda et al. (Masuda et al. 2012) and Yoshida (Yoshida et al. 2012) explained the scour pattern regimes associated with particular Reynolds number ranges and initial distances.

Numerical studies of scour have traditionally treated the sediment bed as a continuum, so the bed load, and if represented, the suspended load, are treated as scalar concentrations. The morphology of the sediment bed is governed by a bed load transport equation and the suspended load is governed by the convection-diffusion transport equation. The majority of the work that uses this bed load approach use either Reynolds Averaged Navier-Stokes (RANS) simulations or Large Eddy Simulation (LES) to model flow. Both numerical methods are covered extensively in the literature, so a detailed review will not be given here. However, it is important to note that these methods model all (RANS) or small-scale (LES) flow structures, and must rely on turbulence models for non-laminar flows. By design, RANS solvers use time-averaged equations. Flow variables are decomposed into two components, the time-averaged value, and the fluctuation. Therefore, RANS solvers cannot accurately predict strongly time-dependent phenomena, like sediment scour. LES essentially applies the flow variables through a low-pass filter, removing the small-scale structures. The large scales of the flow are fully resolved directly, but the small scales are modeled in order to reduce computational cost. Since sediment scour occurs at the interface between the fluid and the sediment bed, exactly where the smallest scales of the flow are generated, LES may be filtering out flow characteristics that are crucial to scouring processes.

Mutlu Sumer (Mutlu Sumer 2007) provides a good general review of mathematical and numerical scour modeling. Tao and Yu (Tao and Yu 2013) have also compiled a thorough and clear review of these methods; a

synopsis of this portion of their review follows. Although there are many variations of the bed load transport equation and approaches to couple the flow to the sediment phase, they are fundamentally similar in that they do not model the individual sediment particles.

Various forms of the bed load methodology have been used extensively in the literature, mostly. Olsen and Melaaen (Olsen and Melaaen 1993), Olsen and Kjellesvig (Olsen and Kjellesvig 1998), Roulund et al. (Roulund et al. 2005), and Liu and Garcia (Liu and García 2008) have simulated wave scour around a large vertical circular cylinder using this technique. Olsen and Melaaen (Olsen and Melaaen 1993) and Olsen and Kjellesvig (Olsen and Kjellesvig 1998) used RANS flow solvers with a $k - \epsilon$ turbulence model, and Van Rijn's bed load concentration formulation (van Rijn 1987) in concert with the convection-diffusion transport equation for sediment concentration. Roulund et al. (Roulund et al. 2005) used a RANS flow solver with a $k - \omega$ turbulence model, and the bed load rate of Engelund and Fredsoe (Frank and Jørgen 1976). Liu and Garcia (Liu and García 2008) simulated 3D flow around a circular pile and 2D wall jet scour. They utilized a RANS flow solver with a $k - \epsilon$ turbulence model and the bed load rate of Engelund and Fredsoe (Frank and Jørgen 1976). Brørs (Brørs 1999), Li and Cheng (Li and Cheng 1999), and Liang et al. (Liang et al. 2005) have used the bed load methodology to simulate the flow and scour below a pipeline, which is represented by a cylinder lying on an erodible sediment bed axially perpendicular to the flow. Brørs (Brørs 1999) used a RANS flow solver with a $k - \epsilon$ turbulence model and a bed load transport rate for a horizontal bed with a slope correction factor. Li and Cheng (Li and Cheng 1999) use a potential flow model and an iterative process to model transient height of the sediment bed using a critical velocity methodology. Liang et al. (Liang et al. 2005) compare the results of a RANS solver with a $k - \epsilon$ closure model against a spatially filtered Navier-Stokes solver with a sub-grid scale (SGS) model. Both solvers are coupled with the bed load rate model of Van Rijn (van Rijn 1987). Hogg et al. (Hogg et al. 1997) simulated a 2D turbulent wall jet over an erodible boundary using a RANS solver and the bed load transport rate of Meyer-Peter and Muller (Meyer-Peter and Müller 1948). Chou and Fringer (Chou and Fringer 2010) used LES and the bed load transport rate of Meyer-Peter and Muller (Meyer-Peter and Müller 1948) to simulate a 3D turbulent boundary layer over an erodible surface.

An alternative numerical approach to the bed load transport method is the Discrete Particle Model (DPM), which is used in this work. The DPM treats the fluid as a continuum and the particles as distinct entities. The model is two-way coupled, whereby the fluid feels the effects of each particle, and each particle feels the

effect of the the surrounding fluid. The model was pioneered by Cundall and Strack (Cundall and Strack 1979). The details of the model are summarized in Section 2.2, following the application by Pepiot and Desjardins (Pepiot and Desjardins 2012). Zhu et al. (Zhu et al. 2007, Zhu et al. 2008) review the theoretical developments of the method and provide a summary of DPM applications and findings. The DPM has many applications, including fluidized beds (see the review of DPM application to fluidized beds by Deen et al. (Deen et al. 2007)) and other particle-fluid flows. However, there has been limited application to the study of scour. Zamankhan (Zamankhan 2009) used LES and DPM to simulate 3D flow over a pipeline, and found good agreement with experimental results.

This paper presents an investigation on the impacts of a vortex dipole on a particle bed, which was conducted using a Direct Numerical Simulation (DNS) code. This particular scenario was selected because it has much practical significance. Vortices that cause erosion are common in the field, as are repeated hydrological events causing subsequent scour and deposition cycles. In the following, the governing equations and numerical method are first briefly summarized, followed by a description of the numerical simulation configuration and set up. The scour characteristics and flow dynamics are then analyzed. Finally, some concluding remarks are presented.

2.2 Governing Equations & Numerical Methodology

The gas/fluid phase is governed by the Low Mach Approximation incompressible Navier-Stokes equations, and the solid phase particles are described by the Discrete Particle Model (DPM), or Lagrangian Particle Tracking (LPT) method, as described by Pepiot and Desjardins (Pepiot and Desjardins 2012). These equations are implemented in an arbitrarily high-order, massively parallel numerical code capable of direct numerical simulations (DNS). This code, NGA, is utilized through a collaboration with its authors, Desjardins et al. (Desjardins et al. 2008).

This code is staggered in both space and time, and, in this work, spatial and temporal integrations are second-order accurate. The scheme conserves mass, momentum, and energy. Time advancement is done using a fractional step Crank-Nicolson scheme. For the full details, the reader is referred to Desjardins et al. (Desjardins et al. 2008) and Pepiot and Desjardins (Pepiot and Desjardins 2012). The following serves as an overview of their methodology.

2.2.1 Gas/Fluid Phase

Taking into account the volume occupied by the particles, the continuity equation is

$$\frac{\partial}{\partial t} \left(\psi_f \rho_f \right) + \nabla \cdot \left(\psi_f \rho_f \mathbf{u}_f \right) = 0 \tag{2.1}$$

where ψ_f is the volume fraction of the fluid, ρ_f is the density of the fluid, and $\mathbf{u}_f$ is the velocity of the fluid. With the addition of a source term for the exchange of momentum with the solid phase, $\mathbf{F}_{inter}$, the conservation of momentum equation becomes

$$\frac{\partial}{\partial t} \left(\psi_f \rho_f \mathbf{u}_f \right) + \nabla \cdot \left(\psi_f \rho_f \mathbf{u}_f \mathbf{u}_f \right) = \nabla \cdot \tau + \mathbf{F}_{gravity} - \mathbf{F}_{inter} \tag{2.2}$$

where $\mathbf{F}_{gravity} = \psi_f \rho_f \mathbf{g}$, and τ is the stress tensor

$$\tau = -p\mathbf{I} + \sigma \tag{2.3}$$

where the pressure is denoted by p and the viscous stress tensor, σ is defined as

$$\sigma = \mu \left(\nabla \mathbf{u}_f + \nabla \mathbf{u}_f^T \right) - \frac{2}{3} \mu \nabla \cdot \mathbf{u}_f \mathbf{I} \tag{2.4}$$

where μ is the dynamic viscosity.

2.2.2 Solid Phase

The location of an individual particle is defined by

$$\frac{d\mathbf{x}_p}{dt} = \mathbf{u}_p \tag{2.5}$$

According to Newton's second law of motion, particles are governed by

$$m_p \frac{d}{dt} \left(\mathbf{u}_p \right) = \mathbf{f}_{inter} + \mathbf{F}_{col} + m_p \mathbf{g} \tag{2.6}$$

where m_p is the mass of the particle, $\mathbf{u}_p$ is the velocity of the particle, $\mathbf{f}_{inter}$ is the exchange of momentum with the fluid for the single particle, and $\mathbf{F}_{col}$ is the force imparted by collisions with other particles or a wall. Since the particles are assumed to be perfect spheres, the particle mass is a function of particle density, ρ_p, and particle diameter, d_p,

$$m_p = \frac{\rho_p \pi d_p^3}{6} \tag{2.7}$$

For a given cell volume, the sum of all of the single particle momentum exchanges, $\mathbf{f}_{inter}$, gives the full momentum exchange term in Equation 2.2

$$\mathbf{F}_{inter} = \sum_i^{N_p} \mathbf{f}_{inter}^i \tag{2.8}$$

The collision term, $\mathbf{F}_{col}$, will be defined in a following section.

2.2.3 Momentum exchange

The momentum exchange between the fluid and a single particle occurs at the surface, S_p, of the particle. Therefore, the interaction force can be calculated by taking the integral of the stress tensor over the surface of the particle. The stress tensor at a specific point is denoted τ', and the momentum exchange term is written as

$$\mathbf{f}_{inter} = \oint_{S_p} \tau' \cdot \mathbf{n} dS \tag{2.9}$$

where $\mathbf{n}$ is unit vector normal to particle surface S_p. Since τ' is not known, but the averaged τ for the cell volume, V, is known, it is assumed that $\tau' = \tau + \mathbf{f}_{drag}$. The drag force, $\mathbf{f}_{drag}$, represents the difference between the average stress tensor value and the value at a specific point. $\mathbf{f}_{drag}$ represents the effect of the particle on the fluid in V.

$$\mathbf{f}_{inter} = \oint_{S_p} \tau \cdot \mathbf{n} dS + \mathbf{f}_{drag} \tag{2.10}$$

Applying the Gauss theorem,

$$\mathbf{f}_{inter} = \int_{V_p} \nabla \cdot \tau dV + \mathbf{f}_{drag} \tag{2.11}$$

The final assumption is that locally averaged stress tensor value will not vary significantly over the scale of a particle diameter, therefore, $\int_{V_p} \nabla \cdot \tau dV \rightarrow V_p \nabla \cdot \tau$. Thus,

$$\mathbf{f}_{inter} = V_p \nabla \cdot \tau + \mathbf{f}_{drag} \tag{2.12}$$

The drag force is formulated as follows

$$\mathbf{f}_{drag} = \frac{18 m_p \mu \psi_f}{\rho_p d_p^2} \left(\mathbf{u}_f - \mathbf{u}_p \right) F \left(\psi_f, Re_p \right) \tag{2.13}$$

Where the function F is Beetstra's (Beetstra et al. 2007) formulation for a dimensionless drag coefficient, which relies solely on the volume fraction of the fluid and the Reynolds number of the particle, $Re_p = \frac{\rho_f d_p |\mathbf{u}_f - \mathbf{u}_p|}{\mu}$:

$$F \left(\psi_f, Re_p \right) = 10 \frac{1 - \psi_f}{\psi_f^2} + \psi_f^2 \left(1 + 1.5 \sqrt{1 - \psi_f} \right) + \frac{0.413 Re_p}{24 \psi_f^2} \left(\frac{\psi_f^{-1} + 3\psi_f \left(1 - \psi_f \right) + 8.4 Re_p^{-0.343}}{1 + 10^{3(1-\psi_f)} Re_p^{-0.5 - 2(1-\psi_f)}} \right) \tag{2.14}$$

In the limit of $\psi_f \rightarrow 1$, Equation 2.14 reduces to

$$F(1, Re_p) = 1 + \frac{0.145 Re_p^{0.656} + \frac{0.413}{24} Re_p}{1 + Re^{-0.5}} \tag{2.15}$$

Although Stokes Law would indicate a value of $F(1, Re_p) = \frac{C_d Re_p}{24}$, Beestra shows that Equation 2.15 compares favorably to other well-known and accepted drag force correlations. The dimensionless drag force coefficient is shown in figure 2.1. This formulation is valid for $Re_p < 1000$. The maximum Re_p in this work is 100.

(a)

(b)
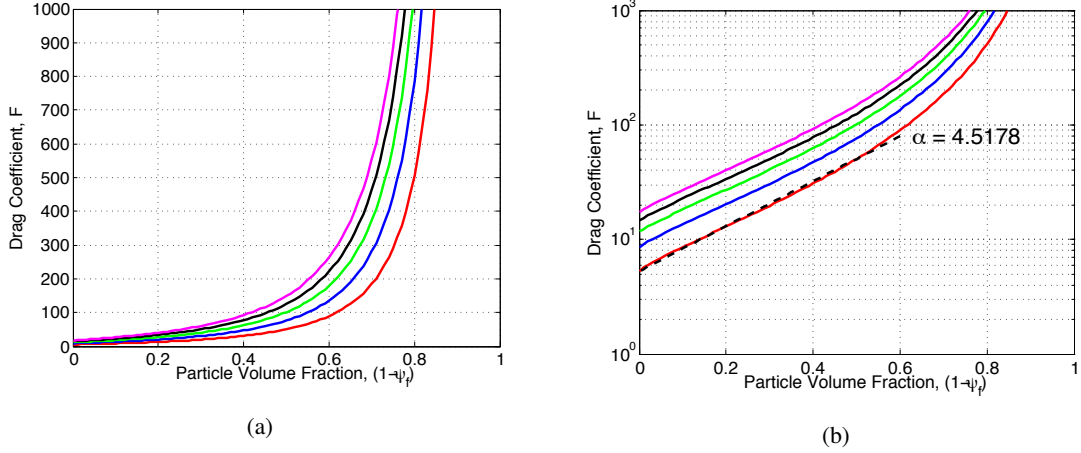
Figure 2.1: (a) Beetstra's drag coefficient for a range of Re_p. (b) Semilog plot of the drag coefficient. $Re_p = 100$ (red), $Re_p = 200$ (blue), $Re_p = 300$ (green), $Re_p = 400$ (black), $Re_p = 500$ (magenta), and power law fit of $Re_p = 100$ (dashed black). In this work, $Re_p = 100$.

2.2.4 Collision Model

A soft-sphere model is used to determine the particle-particle collision forces. The collisions are described by a spring-dashpot model. For any two particles a and b, d_{ab} is the distance between the centers, and r_i is the radius of any particle i. A collision spring force is generated if $d_{ab} < (r_a + r_b + \lambda)$, otherwise, the collision force is zero. The λ buffer region increases the stability of the algorithm, because the collision force is not an instantaneous step function. As a result of this approach, the particles are capable of compression. In this work, a particle bed is constructed and gravity acts to keep it in place. Under no other external forces, the gravitational force and the collision forces in the bed achieve a equiblirium state and the particles are effectively compressed.

$$\mathbf{f}_{col}^{a,b} = (k\delta - \eta(u_a - u_b) \cdot \mathbf{n})) \, \mathbf{n} \tag{2.16}$$

Where k is the spring constant, η is the dashpot damping coefficient, δ is the particle overlap, $\mathbf{u}_i$ is the velocity of any particle i, and $\mathbf{n}$ is the unit vector between the centers of particles a and b. The damping coefficient is

written

$$\eta = -2ln\,e\frac{\sqrt{m_{ab}k}}{\sqrt{\pi^2 + (ln\,e)^2}}, \quad m_{ab} = \frac{m_a m_b}{m_a + m_b} \tag{2.17}$$

Where the restitution coefficient is $0 < e < 1$ and the mass of any particle i is m_i. The total collision force
on a particle i is the sum of the collision forces from all particles j

$$\mathbf{F}^i_{col} = \sum_j \mathbf{f}^{i,j}_{col} \tag{2.18}$$

Particle-wall collisions are determined by treating the wall as a particle, with a radius of zero, and infinite
mass.

2.2.5   Fluid and Solid Coupling

Since the fluid properties are stored on the Eulerian grid and the particles can move anywhere within the La-
grangian framework, properties must be interpolated between the grid and any point occupied by a particle.
Fluid properties are mapped to particle positions using a trilinear interpolation scheme. Alternatively, parti-
cle properties are mapped to the grid using a conservative mollification approach. The mollification kernel
function is defined as

$$\zeta(s) = \begin{cases} \frac{1}{4}s^4 - \frac{5}{8}s^2 + \frac{115}{192}, & \text{if } s \leq 0.5 \\ -\frac{1}{6}s^4 + \frac{5}{6}s^3 - \frac{5}{4}s^2 + \frac{5}{24}s + \frac{55}{96}, & \text{if } s \leq 1.5 \\ \frac{(2.5-s)^4}{24}, & \text{if } s \leq 2.5 \\ 0, & \text{else} \end{cases}$$

where $s = |x|/\delta$ is distance from the center of the particle, normalized by the characteristic length, δ, the
local grid spacing.

The extrapolated interaction force at each surrounding grid point, i, is

$$\mathbf{f}'_{inter,i} = \gamma_i \mathbf{f}_{inter} \tag{2.19}$$

γ normalizes the particle force for all applicable grid points to which it is extrapolated, ensuring that the particle force is conserved when it is applied to the Eulerian grid.

$$\gamma_i = \frac{\int_{V_i} \zeta(s)ds}{\sum_j \int_{V_j} \zeta(s)ds} \tag{2.20}$$

2.2.6   Operating parameters

The DPM places its own set of restraints on the system. In addition to the CFL_f condition associated with the fluid, a CFL_p number is also associated with the particle model. Alone, this restriction limits the particle overlap to 10% of the particle diameter in order to eliminate large overlaps and the large, unphysical, collision forces that would result.

$$CFL_p = \frac{\Delta t_p |u_p|}{d_p} \leq 0.1 \tag{2.21}$$

where Δt is the particle timestep and u_p is the particle velocity. Integration of the particle timestep also requires a restriction due to the characteristic timescale of particle collisions,

$$\tau_{col} = 2\sqrt{\frac{m_{ab}}{k}} \tag{2.22}$$

τ_{col} is used to define k by $\Delta t_p \leq \tau_{col/5}$. In order to maintain computational feasibility, realistic values of τ_{col} can not be used. $\tau_{col/5}$ is used in its place, as per Pepiot and Desjardins (Pepiot and Desjardins 2012). Combined with $CFL_p \leq 0.1$, the particle overlap is limited to a few percent of the particle diameter.

The conservation of mass, Equation 2.1 and conservation of momentum, Equation 2.2, use a locally volume-averaged approach. For the validity of the model, the volume over which quantities are averaged must be an order of magnitude larger than volume of the largest particle it contains, such that $\Delta x^3 \simeq 10 \frac{\pi d_p^3}{6}$. Therefore, the maximum allowable d_p is determined by Δx, which is a function of the smallest scales of the flow.

Although the flow field of the vortex dipole is symmetric and centered on the Eulerian grid, it will be shown that the scour topography does exhibit asymmetrical characteristics. Due to the nature of the DPM, the particles, which make up the bed, are not necessarily centered on the grid. Therefore when the vortex

dipole impacts the bed, one vortex may be inflicting the maximum shear stress directly onto a single particle, while the shear stress of the other vortex is spread between two particles. Because of the coupling between the flow and the particles, and the drag force associated with this impact, the overall effect will not be symmetric. And, once the symmetry is lost, the rest of the simulation, and subsequent impacts will not be able to recapture it.

Additionally, since particle-particle interactions of the DPM utilized in this work are based on a spring-dashpot approach, where the collisions, or even slight particle overlaps due to round-off errors, are corrected by a spring force, the "settled" particle bed is not actually static. To minimize this effect, the spring constant k is adjusted for each Shields number (and, thus, particle density) configuration, in order to achieve particle-particle oscillations that are significantly smaller than the forces inflicted by the vortex dipole. The DPM is extremely sensitive to the spring constant parameter. If k is too small, the particles will effectively collapse onto each other. If k is too large, a static particle bed, under no external forcing, will eventually experience eruptions due to the cumulative effect of the large spring constant. Therefore, a unique spring constant is required for each Shields number (and corresponding particle density). To determine the appropriate k value for a given particle density, a series of simulations are run. These simulations consist of a tightly particle bed subjected only to a gravitational force. The series of simulations are run with incrementally varied k values. The RMS of the particle velocities are calculated, with the minimum RMS corresponding to the appropriate k value for the tested particle density.

2.3 Vortex Dipole Verification

This work simulates the erosion of a particle bed by the repeat impacts of a vortex dipole, which is representative of fundamental turbulent flow structures. Vortex dipoles are characteristic of the structures found in turbulence, like streamwise vortices, and flow past bluff bodies.

2.3.1 Lamb-Oseen Vortex

In this work, the vortex-dipole is based on the Lamb-Oseen vortex:

$$V_\Theta(r) = \frac{\Gamma}{2\pi r} \left(1 - exp\left[\frac{-r^2}{r_c^2} \right] \right) \tag{2.23}$$

Γ is the circulation, r is the radial distance from the center of the vortex, and r_{core}, or r_c, is the radius from the vortex center to its core, at which the circumferential velocity, V_Θ, is a maximum. A cross section of the velocity profile of the Lamb-Oseen vortex can be seen in Figure 2.2a. Only at significant distances from the center of the vortex does the vortex field become negligible. Even at $r/r_c = 50$, the velocity is still over 3% of the maximum V_Θ.

2.3.2 Vortex Dipole

The vortex-dipole is created by combining two lamb-oseen vortices of opposing orientation. Each Lamb-Oseen vortex is shifted an equal distance, x_c, from the center of the domain. With the radial distance, $r = \sqrt{(x \pm x_c)^2 + (y \pm y_c)^2}$, and $y_c = 0$, the shifted Lamb-Oseen vortex flow field equations become:

$$V_\Theta(r) = \pm \frac{\Gamma}{2\pi\sqrt{(x \mp x_c)^2 + y^2}} \left(1 - exp\left[-\frac{(x \mp x_c)^2 + y^2)}{r_c^2}\right]\right) \tag{2.24}$$

And the vortex-dipole equation is simply the sum of these two equation:

$$
\begin{aligned}
V_\Theta(r) = {} & \frac{\Gamma}{2\pi\sqrt{(x - x_c)^2 + y^2}} \left(1 - exp\left[-\frac{(x - x_c)^2 + y^2}{r_c^2}\right]\right) \\
& - \frac{\Gamma}{2\pi\sqrt{(x + x_c)^2 + y^2}} \left(1 - exp\left[-\frac{(x + x_c)^2 + y^2}{r_c^2}\right]\right)
\end{aligned}
\tag{2.25}
$$

A cross-section of the velocity profile of the vortex-dipole is shown in Figure 2.2b. The parameters of the dipole are configured based on the work by Kravchenko et al. (Kravchenko et al. 1993). The statistically averaged distance between streamwise vortices in a turbulent channel flow is roughly three times the core radii of the streamwise vortices. Therefore, the core radius of each vortex of the dipole is $r_c = \frac{1}{3}D$, where D is the diameter of the dipole. The dipole velocity field decays much more rapidly than the velocity field of a solitary vortex. This is due to the opposing orientations of the two vortices, which amplify at the center of the domain (thus driving the vortex dipole), but damp elsewhere.

   The velocity field of the vortex dipole is shown in Figure 2.2c, overlaying a contour plot of the Q factor. Reflecting the velocity profile of Figure 2.2b, the velocity vector field shows a strong downward velocity component at the centerline of the dipole. In conjunction with the weaker components in the rest of the field, the centerline velocity dominates, and the dipole moves downward.

(a)

(b)

(c)
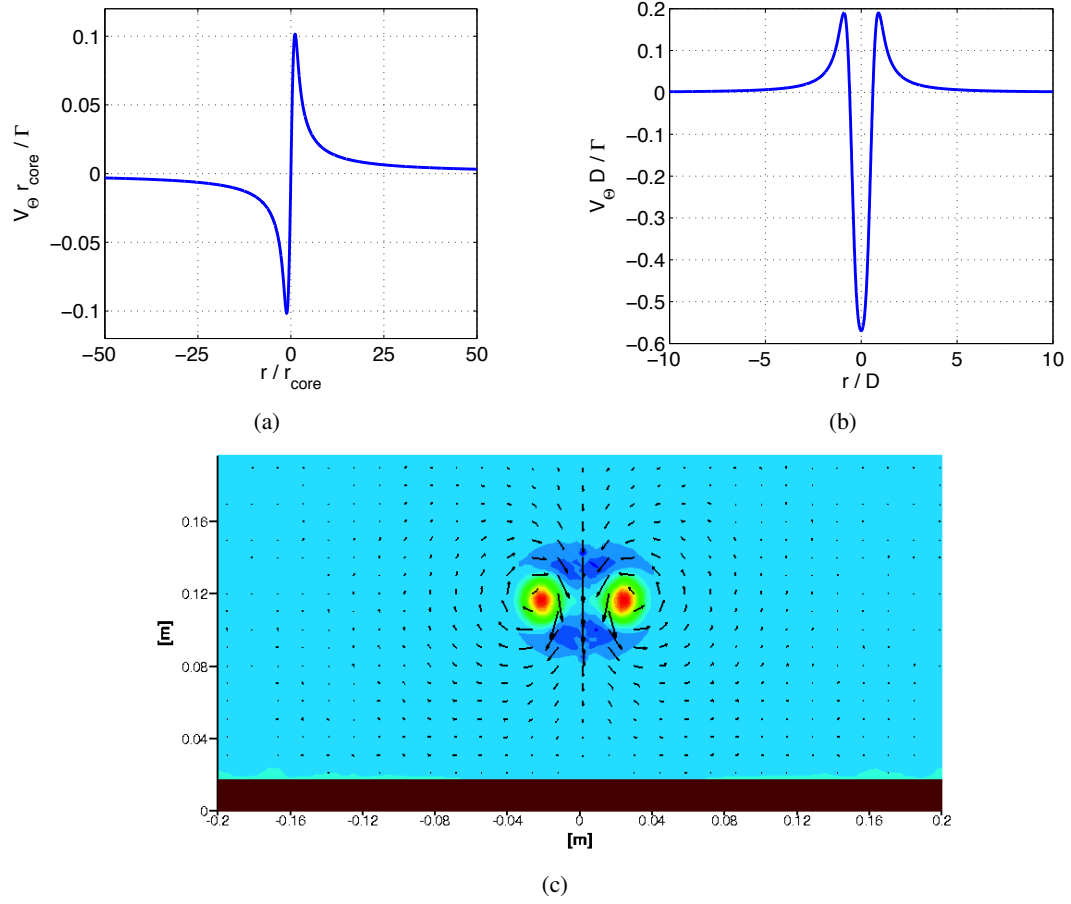
Figure 2.2: (a) Lamb-Oseen vortex velocity profiile cross section. Single vortex centered in domain, spinning counter-clockwise. The maximum velocity occurs at $r = r_{core}$. (b) Vortex-dipole velocity profile cross section. At the center of dipole, the velocity fields amplify, and the net effect is the self-induced downward motion of the dipole. (c) Simulation configuration: the vortex dipole velocity field is overlaid on a surface plot of the Q factor. The particle bed is shown at the bottom of the domain. Only a portion of the full domain is shown.

2.3.3 Verification

To verify the accuracy of the vortex dipole, the parameters used by Lim et al. (Lim et al. 1998), were

duplicated. Lim et al. studied the interaction of a vortex dipole and a wall to investigate the effects of

magnetic fluxes on streamwise vortices. The experiments consist of the vortex dipole impacting the wall with

a propagation direction perpendicular to the wall. The control numerical experiment was conducted in the

absence of any magnetic fluxes. Consistent with Lim et al., the half-domain height is δ, the vortex diameter

is $D = \frac{1}{3}\delta$, and the vortex core radius is $r_c = \frac{1}{9}\delta$. The domain is 6δx2δ in the spanwise and wall normal

directions, respectively. This is slightly narrower than Lim et al. (Lim et al. 1998) who used $2\pi\delta$ in the

spanwise direction. The wall has the no-slip boundary condition, and it is periodic in the spanwise direction.

Figure 2.3 compares results with the control of Lim et al. There is good agreement for the path of the vortices.

In both cases, the vortex dipole begins to separate into two vortices as it gets close to the wall. Once the dipole

makes contact, the two vortices move away from each other as they rebound from the wall. After they have

rebounded, the vortices propagate back towards the original centerline of the dipole before separating again

and dissipating.
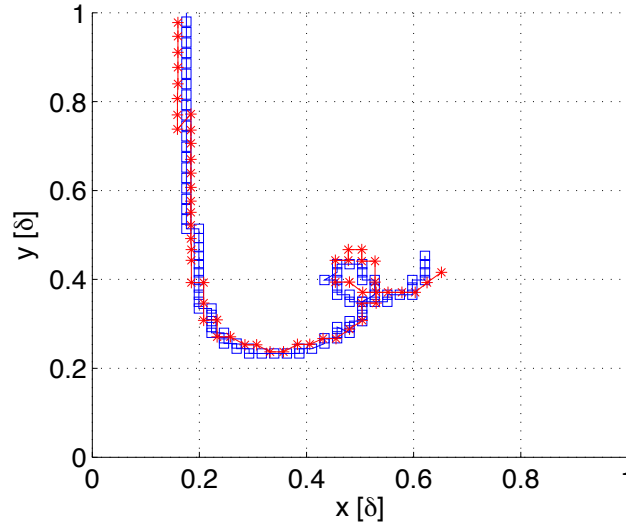
Figure 2.3: Vortex path. The data of Lim et al. is denoted by red asterisks, and the data from this work is
denoted by blue squares. The horizontal axis is the wall, and the vertical axis represents the centerline of the
dipole. The units are normalized by the channel half width, δ. The vortex impacts the wall and rebounds,
but the self-induced motion causes a second impact before the vortex dissipates due to viscous effects. The
location of the vortex core is determined by the location of the maximum Q value.

2.4   Simulation Configuration & Methodology

The parameters of the vortex dipole are configured based on the work by Kravchenko et al. (Kravchenko et al. 1993). The statistically averaged distance between streamwise vortices in a turbulent channel flow is roughly three times the core radii of the streamwise vortices. Therefore, the core radius of each vortex of the dipole is $r_c = \frac{1}{3}D$, where D is the diameter of the dipole, see Figure 2.4 for a schematic of the initial configuration of the simulation. The domain is $6\delta \times 2\delta$ in the spanwise and wall normal directions. This is slightly narrower than Lim et al. who used $2\pi\delta$ in the spanwise direction. There are 256 spanwise nodes and 150 wall-normal nodes. This grid configuration allows for particle diameters of $1000\mu m$ while meeting the $\Delta x/d_{particle}$ criteria described in Section 2.2.6. The wall at the bottom of the domain has a no-slip boundary condition and is covered in a layer of particles, held in place by the gravitational force, acting in the negative y direction. The particle bed comprises 20 layers of tightly packed particles, per Figure 2.4, resulting in 18,000 total particles. The domain is periodic in the spanwise direction.
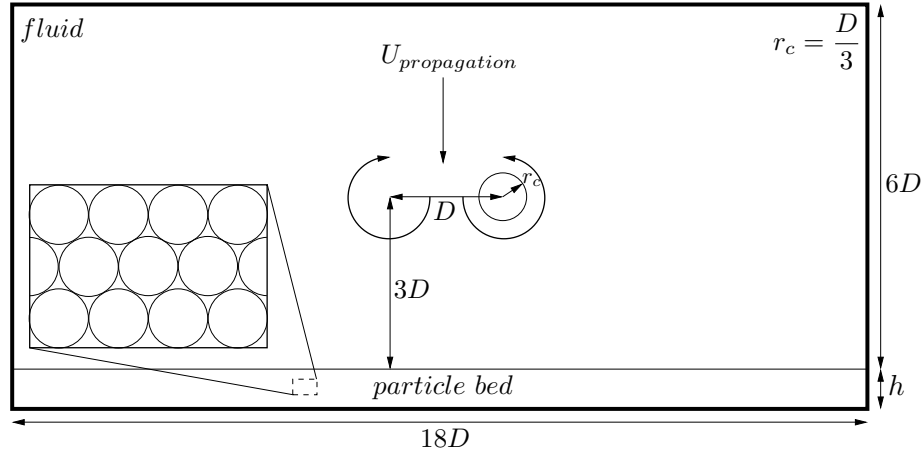
Figure 2.4: Initial configuration of the simulation. The vortex dipole is centered in the domain, starting $3D$ from the particle bed. The core of each vortex is located at a distance $r_c = D/3$ from vortex centers. The bed is comprised of particles in a tightly packed formation to a height of h.

To conduct the study of the repeated impacts of the vortex dipole onto the particle bed, the following methodology is followed.

1. Despite building the particle bed so that the particles are closely packed, the bed must settle further under the effect of gravity, such that the particles are slightly compressed onto the wall. In order to

make sure that this process is isolated from any erosive behavior caused by the vortex dipole, the bed
must be allowed to settle under the effect of gravity alone. Therefore, the full simulation domain is
initialized with a zero velocity field. The particles then settle into an equilibrium state with the effect of
gravity and the bottom wall. Since the bed is initialized in a close-packed structure, the settling process
only compressed the particles, but does not cause reshuffling. The final, settled, particle bed is stable
and level.

2. Once the particle bed has settled, the vortex dipole is initialized and collides with the settled, and non-
scoured, particle bed. For cases in which scouring is observed, the vortices either entrain the particles
into the fluid or force them to slide on top of one another. The simulation is run until all of the particles
have been re-deposited to the surface by the gravitational force and the vortices separate and dissipate
(ensuring that further erosion will not occur). The evolution of a typical system is illustrated in Figure
2.5.

3. The newly scoured bed is retained and the flow field is reset to that of the original vortex dipole. This
second dipole impacts the scoured bed. Again, the particles are allowed to settle and the vortices to
dissipate.

4. Step 3 is repeated for a total of 5 impacts.

Steps 1-4 are repeated for a range of the Shields numbers, $\Theta = \tau_{bed}/(\rho_{particle} - \rho_{fluid})gd_{particle}$, which is
the ratio of the fluid shear stress at the bed to the gravity force. The critical value of the Shields parameter,
Θ_c, is the threshold beyond which incipient bed particle motion is observed. The repeated impacts were
conducted at Θ/Θ_c of 1, 1.5, 3, and 4.5. Munro et al. (Munro et al. 2009) used Shields number in the
range of 1 through 10 to achieve their scour patterns. The Reynolds number of the vortex dipole is defined
as $Re_U = UD/\nu$, where U is the propagation velocity of the dipole, D is the dipole diameter, and ν is the
kinematic viscosity of the fluid. All simulations were conducted with a Reynolds number of 5600, which is
right in the middle of the range used by Munro et al. (Munro et al. 2009) in their experiments. Both gravity,
$g = -9.81\,m/s^2$, and the particle diameter, $d = 1000\,\mu m$, are constants. Therefore, in order to alter Θ,
the particle density is modified, per Table 2.1. A standard assumption of sediment density is roughly 2700
kg/m^3. However, in order to utilize a lower Reynolds number flow, and thus larger grid spacing (per Section
2.2.6), lower densities were required.

(a) $t = 1.0$ sec

(b) $t = 1.6$ sec

(c) $t = 2.2$ sec

(d) $t = 2.8$ sec

(e) $t = 3.4$ sec

(f) $t = 4.0$ sec
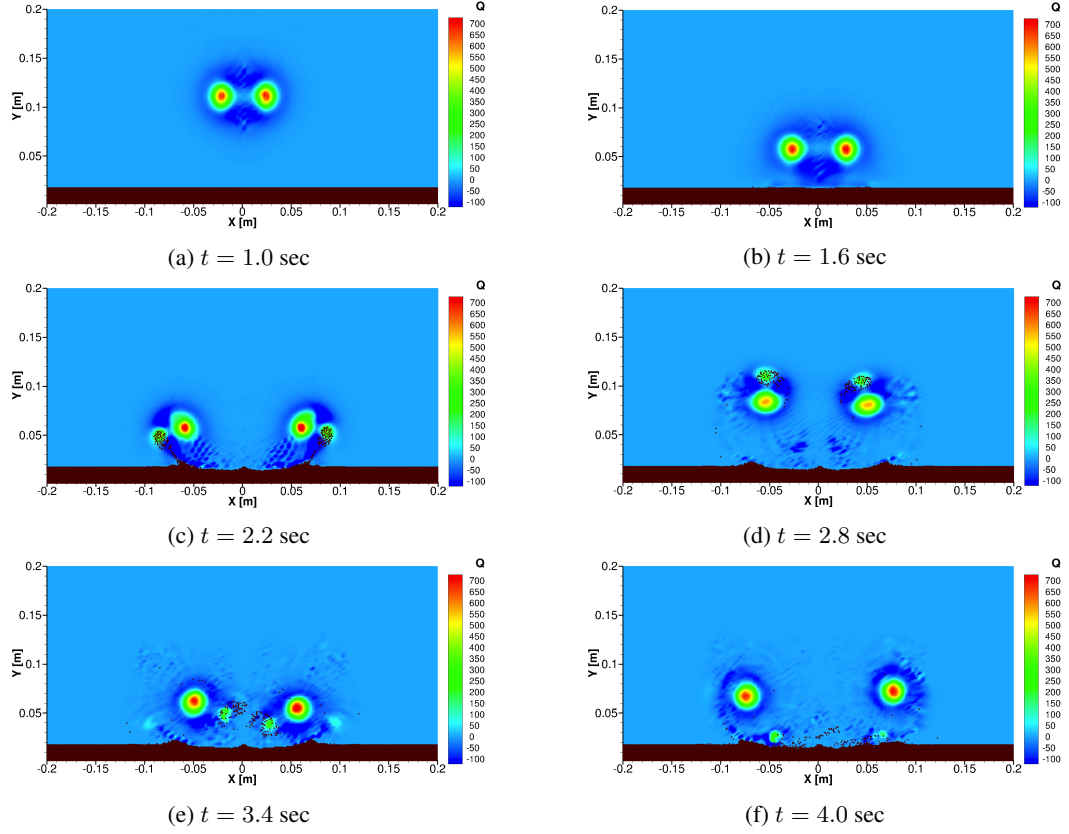
Figure 2.5: The vortex dipole propagates downward until it impacts the particle bed. Much like a vortex dipole impacting a wall, the vortices rebound from the wall, but since the wall is a particle bed in this case, particles are entrained into the fluid. The effect of gravity pulls the entrained particles back to the bed, the vortices eventually separate and dissipate, and a scoured bed topography is left. The Shields number is $\Theta/\Theta_c = 4.5$.

$\rho_{particle}$ $[kg/m^3]$	2500	2200	**1900**	1600	1300	1200
Θ/Θ_c	0.6	0.75	**1**	1.5	3	4.5

Table 2.1: The Shields number is modified by changing the particle density, $\rho_{particle}$. At the critical Shields number, $\Theta/\Theta_c = 1$, the particle density is 1900 kg/m^3 (which is highlighted in bold).

2.5 Results

2.5.1 Scour Hole Characteristics

The observed scour hole topography resulting from the impact of the initial vortex dipole displays universal
characteristics at all Shields numbers. At Shields numbers above the critical value, some particles become
entrained in the fluid of the vortex and are swept away from the bed. Particles that are near the impact zone,
but are not entrained, are swept to each side of the scour hole, forming mounds. This process is shown in
Figure 2.5 for $\Theta/\Theta_c = 4.5$. As can be seen in Figure 2.6, the impacts of the initial dipole, for all Shields
numbers above the critical value, yield a similar surface topography, whereby each vortex sweeps away a "u"
shape, resulting in a "w" shape overall. The scour hole displays a local maximum, or peak, at the center of
the hole, and a mound is formed on each side of the hole. Even at the critical Shields number, where incipient
particle motion is observed, and below which no particles are dislodged, this phenomena is observed, albeit
at a smaller scale. Because the relative effect of the gravitational force is so strong, the vortex dipole manages
to push only a few particles up and over their neighbors, but the particles never become entrained in the fluid.
The maximum scour hole is generally observed directly below either of the vortices in the dipole, where the
shear bed stress is at a maximum. At higher Shields numbers, the entrained particles may fall back into the
scour hole. Therefore, the scour hole shape is not necessarily smooth.

The bed shear stress at the fluid-bed interface is shown in Figure 2.7, for the first vortex dipole impact
at $\Theta/\Theta_c = 4.5$. The bed shear stress is shown at time $t = 1.5$ seconds, as the dipole begins to impact
the wall. Maximums are found below each vortex of the dipole, with the bed shear stress decaying to zero
towards the edges of the domain. The bed shear stress is also zero at the centerline of the vortex dipole, which
corresponds to the local maximum in the scour hole topography.

The evolution of the scour hole topography with successive impacts is shown in Figure 2.8. At the critical
Shields number, shown in Figure 2.8a, the scour topography and maximum depth are not significantly altered
with subsequent impacts of the vortex dipole. The topographies formed after each of the three impacts show
the characteristic removal of particles at the points of impact, and the formation of mounds to each side of the
scour hole. In this case, the "hole" and "mounds" are only a single particle diameter in magnitude, but they
are observed. At a moderate Shields number of $\Theta/\Theta_c = 1.5$, the scour hole pattern is mostly retained after
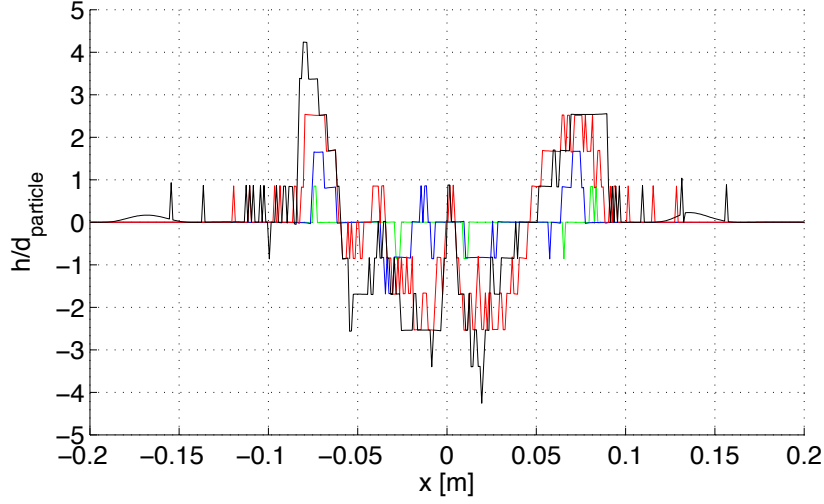
Figure 2.6: Scour topographies resulting from the impacts of the initial vortex dipoles. The Shields number is indicated by the line color: $\Theta/\Theta_c = 1$ (green), $\Theta/\Theta_c = 1.5$ (blue), $\Theta/\Theta_c = 3$ (red), $\Theta/\Theta_c = 4.5$ (black). Scour hole is normalized by the particle diameter. At the critical Shields number, the scouring is minimal, but the erosion is present in the center and peaking at the sides. At higher Shields numbers, these characteristics are exaggerated, with a much larger scour hole and correspondingly large mounds at each side.

each impact. A local maximum is observed in the scour hole and a mound is formed at each side of the hole.

At higher Shields numbers, $\Theta/\Theta_c = 3$ and $\Theta/\Theta_c = 4.5$, the first two impacts display the characteristic scour hole pattern of the lower Shields number simulations, but with greater magnitude. Figures 2.8c and 2.8d show much more exaggerated scour hole depths, peaks within the holes, and mounds to the sides of the holes. Noticeably, in both cases, the topography of the scour holes are significantly different after the third impacts. The local maximum peak in the scour hole is either shifted off center or no longer present. This phenomenon is due to the interaction of the vortices with the exaggerated characteristics of the scour hole topography after the second impact. The vortices have achieved significant scour hole depths, and correspondingly, the mounds that have formed on the sides of the hole are significantly high, eclipsing the $4d_{particle}$ mark. The significant scour hole depth and mound height alter the ability of the vortex dipole to follow its regular trajectory. This phenomena is discussed in Section 2.5.2.

In order to quantify scour hole topography, the roughness, R is calculated here as the root-mean-square (RMS) of the fluid-bed interface location, normalized by the particle diameter. Figure 2.9 shows that R varies by only a percent or two over the entire Shields number parameter space. As the scour hole topographies would indicate at the lower Shields numbers, R is not altered appreciably with subsequent impacts. The

(a) Bed shear stress

(b) Maximum bed shear stress
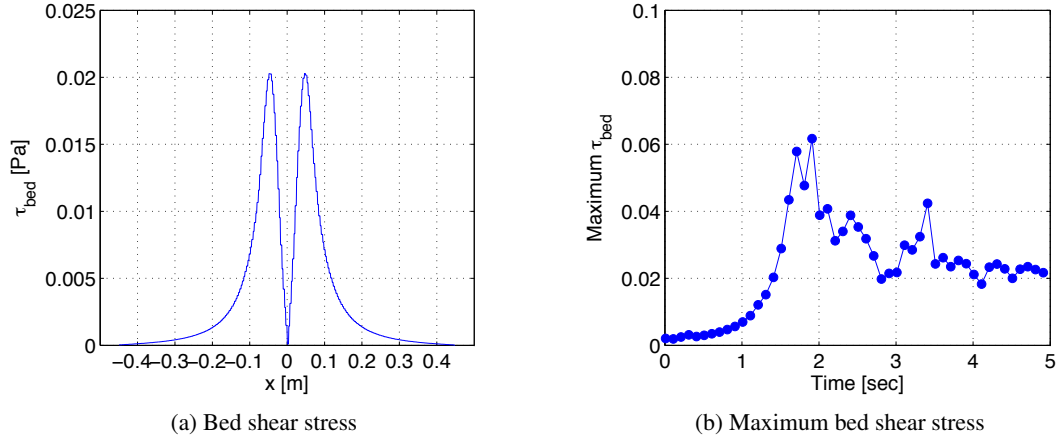
Figure 2.7: (a)Bed shear stress, τ_{bed}, at time 1.5 seconds, $\Theta/\Theta_c = 4.5$. The two maximums correspond to the two vortices that comprise the dipole. τ_{bed} decays to zero as the distance from the vortex dipole centerline increases. τ_{bed} also goes to zero at the dipole centerline, since the symmetry of the flow results in only a vertical velocity component at this location. (b) Maximum bed shear stress.

higher Shields numbers show increases in scour hole roughness with subsequent impacts, but the scale of the increase is still minimal.

There are two scour hole depth regimes. As shown in Figure 2.10a, the first regime contains the three lowest Shields numbers, Θ/Θ_c of 1, 1.5, and 3. In this regime, the maximum scour hole depth, h, is unchanged by the impact of the third vortex dipole. After the second impact, the shape of the scour hole has reached an equilibrium state with the scouring flow structure. The scour hole depth is approaching, or has reached, its asymptotic limit. Additional impacts may alter the scour topography, but the maximum scour hole depth will not change. The second regime is characterized by the higher Shields number of $\Theta/\Theta_c = 4.5$ and a non-linear increase in the maximum scour hole depth by the impact of the third dipole.

However, the two scour hole depth regimes are not as clearly defined as they appear. The maximum scour hole depth observed after the impact of the second vortex dipole is the same for the $\Theta/\Theta_c = 3$ and $\Theta/\Theta_c = 4.5$ cases. However, at $\Theta/\Theta_c = 3$, the impact of the third vortex does not have any effect on the maximum scour hole depth, while at $\Theta/\Theta_c = 4.5$, the scour hole depth increases non-linearly.

Since the maximum scour hole depth alone cannot provide a full picture of the scour dynamics, the scour hole topography and total mass lost is quantified. The number of particles removed below the original height of the particle bed serves as the measure of mass loss due to the scouring process. This value is denoted here

(a) $\Theta/\Theta_c = 1$

(b) $\Theta/\Theta_c = 1.5$

(c) $\Theta/\Theta_c = 3$

(d) $\Theta/\Theta_c = 4.5$
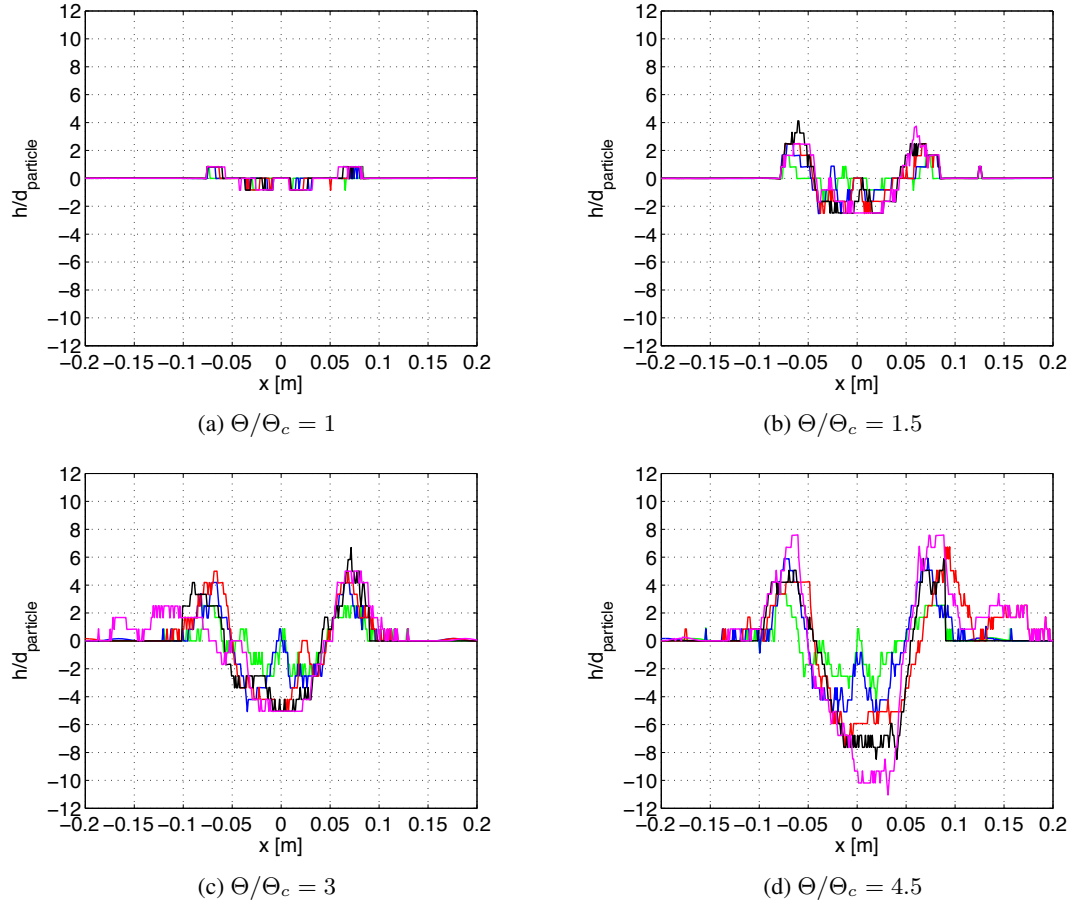
Figure 2.8: Scour hole topography for the range of Shields numbers examined. The impact number is indi-
cated by the color of the line: 1st (green), 2nd (blue), 3rd (red), 4th (black), 5th (magenta). The depth of the
scour hole is non-dimensionalized by the diameter of the bed particles. (a) At the critical Shields number,
the flow is only able force a few particles to slide over neighboring particles. (b)-(d) At higher numbers,
the characteristic "w" scour hole shape is created, each "u" formed by one of the two vortices. The eroded
particles are forced into mounds, or peaks, which surround the scour hole.

Figure 2.9: Scour hole roughness. The Shields number is indicated by the line color: $\Theta/\Theta_c = 1$ (magenta), $\Theta/\Theta_c = 1.5$ (black), $\Theta/\Theta_c = 3$ (blue), $\Theta/\Theta_c = 4.5$ (green). The RMS of the fluid-bed interface location, normalized by the particle diameter.

as the scoured volume, ΔV. Contrary to what the maximum scour hole data implies, Figure 2.10b shows that

the rate of mass loss is very nearly linear for all Shields number through the series of three impacts.

2.5.2 Flow Dynamics

As discussed in Section 2.3.3, a vortex dipole impacting a solid wall is expected to rebound and then dissipate.

This type of behavior can be clearly seen in Figures 2.12a and 2.12b, which are subcritical Shields numbers.

Therefore, no scouring occurs, and the trajectories of subsequent dipole impacts do not change, because

the bed itself has not changed. However, as the Shields number increases above the critical threshold, as

in Figures 2.12c and 2.12d, the trajectories do begin to change with increasing number of impacts. But,

since the scouring is minimal in the case of the $\Theta/\Theta_c = 1$, and modest in the $\Theta/\Theta_c = 1.5$ case, the

topography does not significantly alter the vortex trajectories. At $\Theta/\Theta_c = 1.5$, the mounds are modest in

size, and, counterintuitively, actually increase the separation of the vortices. During the initial impact, the

vortices propagate back towards the centerline two times, instead of one. However, during the second and

third impacts, the mounds formed during the initial impact act to separate the vortices of the dipole. The

vortices are able to crest the mound and fall to the outside of the scour hole. Once this happens, the vortices
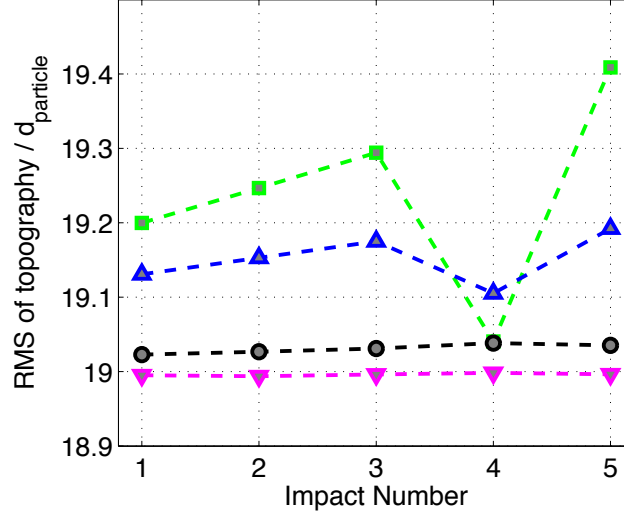
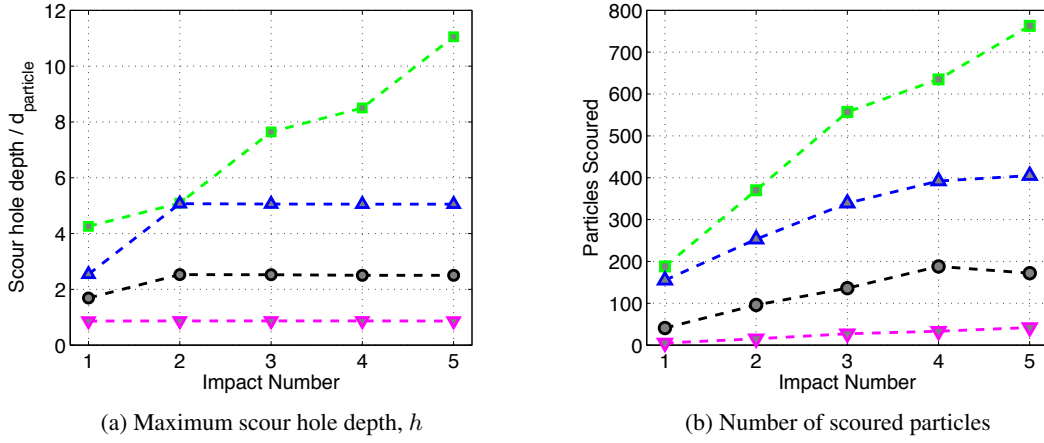(a) Maximum scour hole depth, h (b) Number of scoured particles

Figure 2.10: The Shields number is indicated by the line color: $\Theta/\Theta_c = 1$ (magenta), $\Theta/\Theta_c = 1.5$ (black), $\Theta/\Theta_c = 3$ (blue), $\Theta/\Theta_c = 4.5$ (green). (a) Scour hole depth h, normalized by the particle diameter. At Θ/Θ_c of 1, 1.5, and 3, the scour hole depth does not increase with the third impact. However, at a Θ/Θ_c of 4.5, a non-linear increase in the scour hole depth is observed. (b) Number of particles removed from scour hole. The volume removed by the scouring process is determined by how many particles have been removed below the original height of the bed. The number of scoured particles increases steadily for all Shields numbers.

are permanently separated, and proceed to dissipate. At high Shields numbers, the increased magnitude of the scour hole mounds, formed by the second impacts, now act to constrain the vortices. As shown in Figures 2.12e and 2.12f, the trajectories of the third vortices no longer indicate separation, but containment much closer to the centerline. In the case of the highest Shields number $\Theta/\Theta_c = 4.5$, it can be seen that the trajectory of the third impact not only is constrained but results in a vortex location equal to that of the original vortex dipole. In both high Shields number cases, the containment of the vortices by the scour hole mounds results in a recombining of the two vortices and a reformation of the vortex dipole. The reformed vortex dipole is no longer symmetric in strength or alignment, and will no longer impact perpendicularly with the bed. Therefore, the resulting scour topography is quite unpredictable and can result in a non-linear increase in the maximum scour hole depth. Figure 2.11 shows the strong asymmetry of the reformed dipole behavior and the resulting interaction with the particle bed.

Since the motion of the flow field is entirely self-induced, the energy of the vortex dipole must decrease with time. Although the vorticity, ω, of the vortex dipole is not a direct analog to its energy, it is also expected that the vorticity should decrease with time. However, the vorticity of each vortex in the dipole may display local increases in magnitude, especially when interacting with the particle bed, or in the case that the vortices
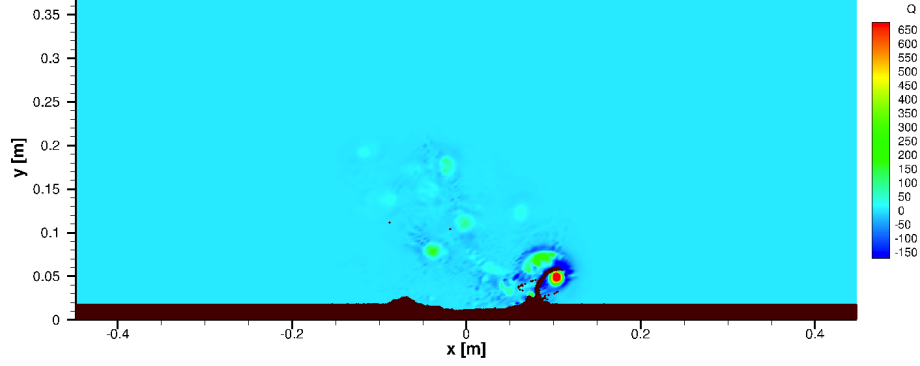
Figure 2.11: The third impact for case $\Theta/\Theta_c = 4.5$. At $t = 11.1$ seconds, the vortices have recombined and re-impact the particle bed. However, due to the asymmetry of the scour hole, the propagation direction of the newly formed dipole is no longer perpendicular to the surface of the particle bed. The new dipole eventually propagates parallel to the bed, rolling up particles as it moves, leaving a strongly asymmetric scour pattern.

recombine to reform the dipole. As shown in Figure 2.13, the evolutions of vorticity are shown to slightly decrease with time overall, but large maxima and minima are observed.

Figure 2.14 plots the path of the vortex core for the first impact, for all Shields numbers, where the core location is colored by the vorticity. The two local maxima peaks ($t \simeq 2.5$ seconds and $t \simeq 3.5$ seconds) in Figure 2.13 correspond to when the vortex is rebounding from its first impact with the wall, and when the second impact of the vortex on the wall is imminent. In between these two occurrences, there is a large drop in vorticity. Vorticity production at a wall has been observed by Kramer et al. (Kramer et al. 2007). Kramer et al. found that vorticity can be produced locally at a no-slip boundary. In this work, the boundary is the surface of the particle bed, which is not strictly no-slip, but is capable of sustaining sufficient stress for vorticity production. For a domain with no-slip boundaries, Kramer et al. provide the equation for the change in total enstrophy, $\Omega = \frac{1}{2} \int_s \omega^2 ds$, which is a measure of the squared vorticity.

$$\frac{d\Omega}{dt} = -\nu \int_D |\nabla \omega|^2 dA + \nu \oint_{\partial D} \omega(\mathbf{n} \cdot \nabla \omega) ds \tag{2.26}$$

ν is the kinematic viscosity, D is the domain, and $\mathbf{n}$ is the unit normal vector at the surface. The first term on the righthand side will always dissipate enstrophy. The second term on the righthand side has the potential to generate enstrophy. This term represents the vorticity influx at the no-slip boundary, and would go to

(a) $\Theta/\Theta_c = 0.6$

(b) $\Theta/\Theta_c = 0.75$

(c) $\Theta/\Theta_c = 1$

(d) $\Theta/\Theta_c = 1.5$

(e) $\Theta/\Theta_c = 3$

(f) $\Theta/\Theta_c = 4.5$
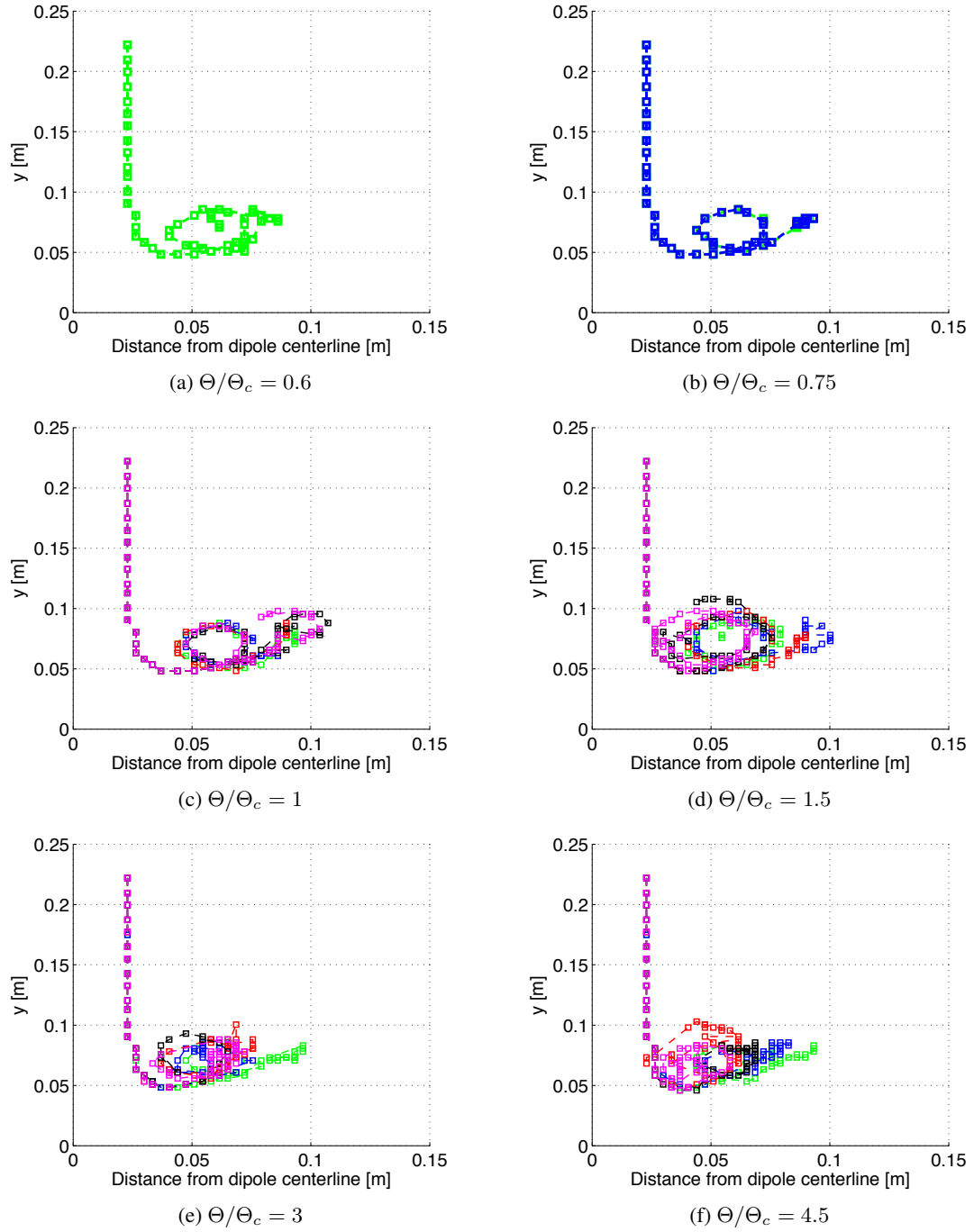
Figure 2.12: Trajectory of one of the two vortices of the vortex dipole, for a range of Shields numbers.
The impact number is indicated by the color of the line: 1st (green), 2nd (blue), 3rd (red), 4th (black), 5th
(magenta). (a)-(b) For subcritical configurations, $\Theta/\Theta_c = 0.6$ and $\Theta/\Theta_c = 0.75$, no scouring is observed,
therefore the vortex trajectory is not altered by subsequent impacts. (c)-(d) At low Shields numbers, the
vortex trajectories are not significantly altered with subsequent impacts. (e)-(f) At higher Shields numbers,
the separation of the vortices is reduced as the number of impacts increase.

(a) $\Theta/\Theta_c = 1$

(b) $\Theta/\Theta_c = 1.5$

(c) $\Theta/\Theta_c = 3$

(d) $\Theta/\Theta_c = 4.5$
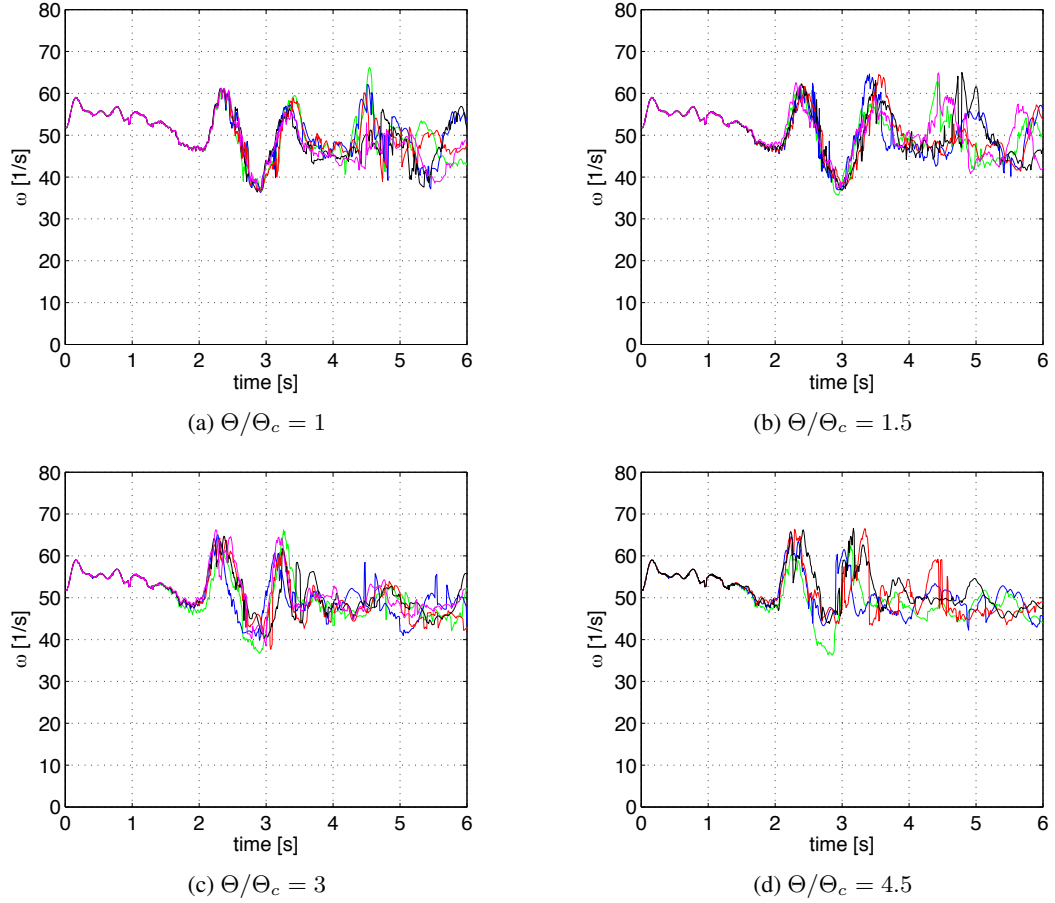
Figure 2.13: Vorticity. The impact number is indicated by the color of the line: 1st (green), 2nd (blue), 3rd (red), 4th (black), 5th (magenta). The decay in vorticity is nearly identical for all systems until roughly $t = 2$ seconds.
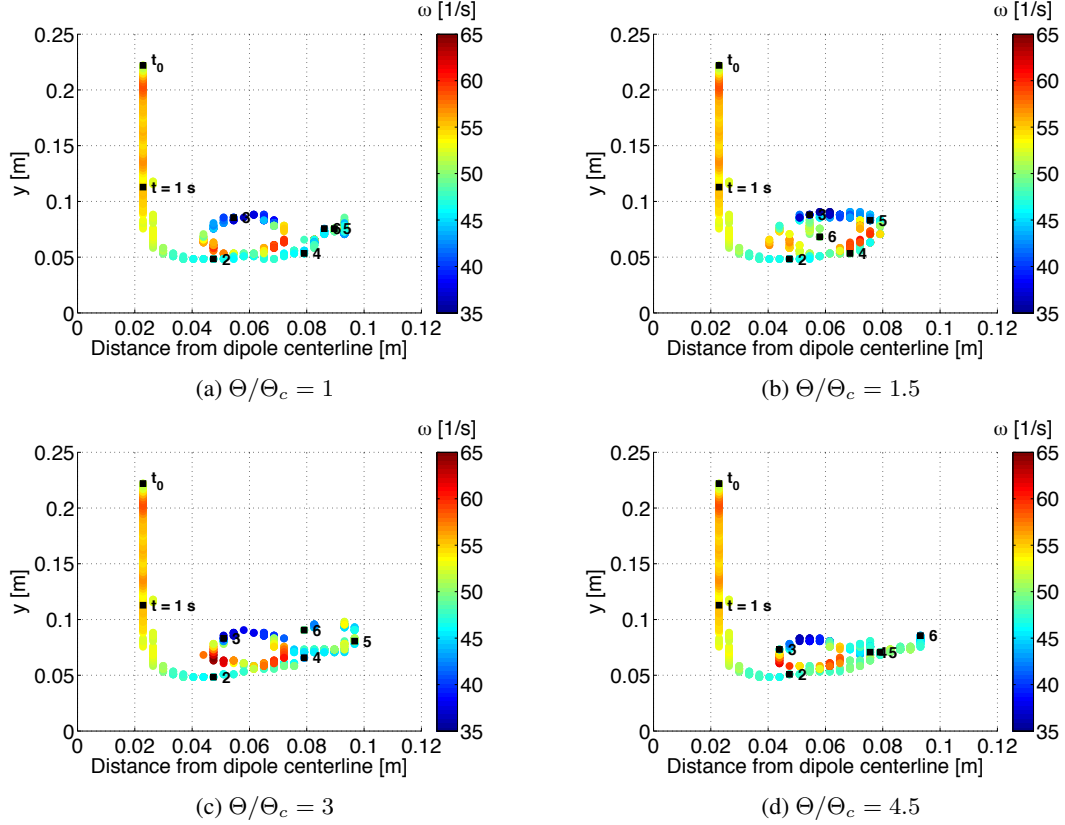
Figure 2.14: Vortex core path of first impact. The core locations are colored by the vorticity of the vortex. The vorticity drops upon impact with wall.

zero in the absence of a no-slip boundary condition. This term becomes positive at $t \simeq 2.5$ s and $t \simeq 3.5$ seconds because ω and $\mathbf{n} \cdot \nabla \omega$ are both either positive or negative. At $t \simeq 3$ s, when ω drops precipitously, ω and $\mathbf{n} \cdot \nabla \omega$ have different signs, and thus the second term on the righthand side of Equation 2.26 becomes negative.

The deviation of vortex core trajectory is measured by comparing the vortex core paths of consecutive impacts. This deviation is calculated by the norm of the difference between the vortex core locations from different impacts. Over the Shields number parameter space, the vortex core path of the first impact is compared to the path of a sub-critical Shields number impact, where no scouring occurs. Subsequent impacts are compared to the previous impact (the second impact is compared to the first impact, the third impact is compared to the second impact, etc.) There is no deviation of the vortex core path as the vortex dipole propagates perpendicularly towards the wall before the first impact. Once the dipole makes contact with the

wall, the vortex core paths begin to deviate. The time at which this occurs depends on the Shields number. In Figure 2.15, path deviation is observed more quickly for higher Shields numbers, presumably because the vortices are more capable of entraining particles and scouring the bed, resulting in modified flow dynamics and an altered bed interface boundary condition.

At the critical Shields number, the first impact shows the greatest deviation. All four subsequent impacts show smaller deviations than the first, with the magnitudes generally decreasing as the number of the impact increases. As has been shown, at $\Theta/\Theta_c = 1$, the maximum scour hole depth does not increase with subsequent impacts, and the increase in the number of scoured particles is slight. Thus the fluid-bed interface topography does not change significantly with subsequent impacts, and therefore, it is expected that path deviations will not be altered significantly as well.

At $\Theta/\Theta_c = 1.5$, the initial impact shows a large peak in deviation. The deviations of the second and third impact are generally smaller in magnitude. However, by the fourth and fifth impacts, the magnitude of the path deviation has begun to increase. The size of the scour hole and mounds has reached the threshold above which the vortices are unable to separate due to the confining effects of the the scour hole mounds. The result is larger deviations in vortex trajectories.

At $\Theta/\Theta_c = 4.5$, the second impact shows a smaller deviation than the first impact, but the third impact shows a larger peak magnitude deviation than either of the two previous impacts. Like the $\Theta/\Theta_c = 1.5$ case, by the third impact, the scour hole depth and mound heights have increased to a size which does not allow the vortices of the dipole to separate. In this case, the scour hole depth and mounds are large enough in magnitude that the dipole reforms quickly, resulting in drastic deviation of the vortex core path from the previous impact.

2.6 Conclusion

A particle bed was subjected to a series of impacts by a vortex dipole, for a Shields number parameter space ranging from the critical value, to 4.5 times the critical value. The scour topography showed a universality for all Shields numbers, particularly after the earlier impacts. At higher Shields numbers, the magnitude of the scour hole characteristics became large enough to significantly alter the behavior of the vortex dipole. The result was a deviation from the symmetry of the universal scour hole shape. The maximum scour hole depth

(a) $\Theta/\Theta_c = 1$

(b) $\Theta/\Theta_c = 1.5$

(c) $\Theta/\Theta_c = 3$

(d) $\Theta/\Theta_c = 4.5$
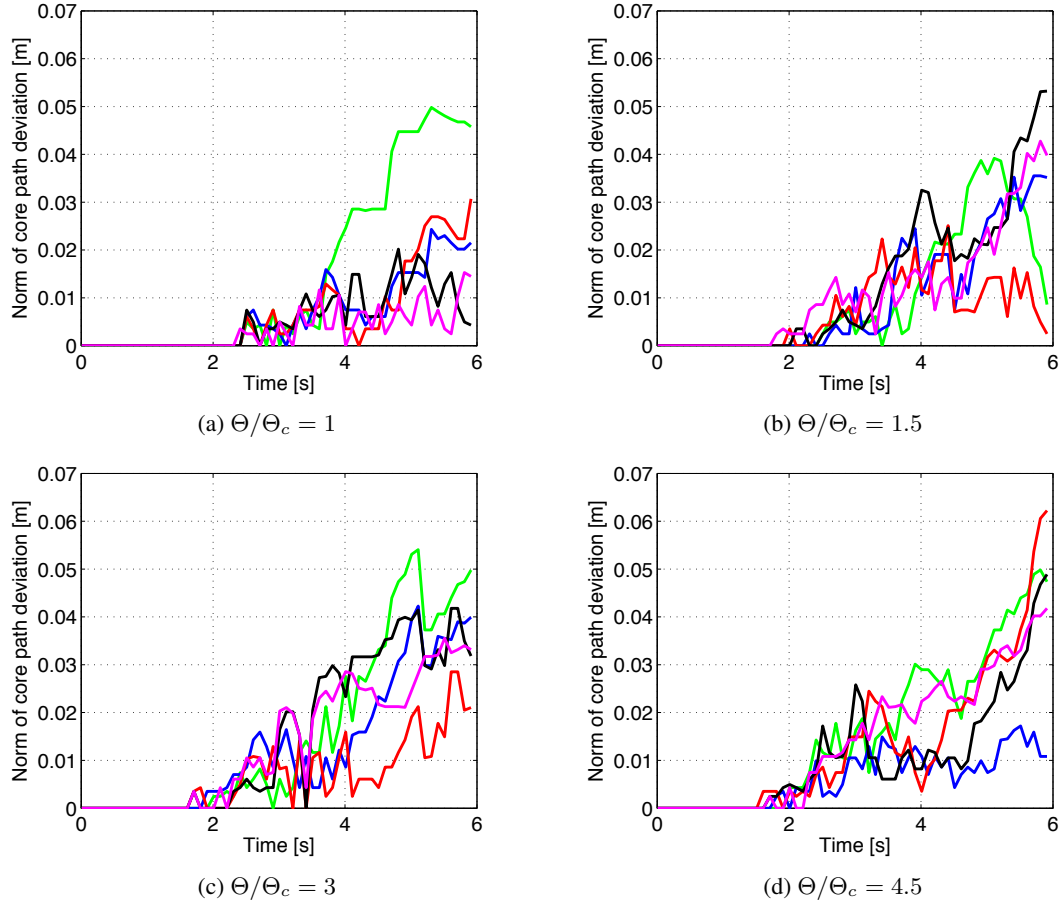
Figure 2.15: Deviation of the vortex core path. The impact number is indicated by the color of the line: 1st (green), 2nd (blue), 3rd (red), 4th (black), 5th (magenta). The first impact is compared to a sub-critical Shields number impact (no scouring is observed). Subsequent impacts are compared to the previous impact (i.e. The second impact is compared to the first impact, the third impact is compared to the second impact, etc.)

is found to be a good indicator of the corresponding vortex dipole behavior, but the total number of scoured particles is a better reflection of the severity of the scouring. Due to the smaller scour hole at the critical Shields numbers, the deviation of the vortex core paths shrank with subsequent impacts. At higher Shields numbers, the deviation of the first vortex core path (which was compared to the path of a sub-critical Shields number vortex dipole, which did not cause any scouring) was larger than deviation of the second impact (and sometimes the third impact, depending on the Shields number). However, once the scour hole developed past a certain scale, the scour hole would dramatically alter the path of the vortex, resulting in large deviations of the vortex core path.

The numerical simulations in this work utilize an Euler-Lagrange approach to investigate repeat scour events. The vast majority of the numerical studies of scour, or erosion, model the coupling between the fluid and the sediment using continuum approaches. This work uses the Discrete Particle Method, which discretely models each individual particle. This approach has been used mostly in research related to fluidized beds and systems displaying similar dynamics, but only sparingly in work related to scour. This work is one of the first to investigate scour through the two-coupling between the fluid phase and solid phase by directly modeling individual particles. In addition, to our knowledge, this work is the first to study the effects of repeated scouring events.

Acknowledgments

Bibliography

Barbhuiya, A. K. and S. Dey (2004). Local scour at abutments: A review. In *Sadhana: Academy Proceedings in Engineering Sciences*, Volume 29, pp. 449–476. Indian Academy of Sciences.

Beetstra, R., M. Van der Hoef, and J. Kuipers (2007). Drag force of intermediate reynolds number flow past mono-and bidisperse arrays of spheres. *AIChE Journal 53*(2), 489–501.

Betts, A. (2011). Climate change in Vermont. Technical report, Vermont Agency of Natural Resources. Climate Change Adaption White Paper Series.

Bove, I., D. Acosta, N. Gutiérreza, V. Gutiérreza, and L. Sarasúa (2013). Double scouring by turbulent jets downstream of a submerged sluice gate. *arXiv preprint arXiv:1311.4194*.

Breusers, H. and A. J. Raudkivi (1991). *Scouring*. AA Balkema Rotterdam,, The Netherlands.

Brørs, B. (1999). Numerical modeling of flow and scour at pipelines. *Journal of Hydraulic Engineering 125*(5), 511–523.

Chatterjee, S., S. Ghosh, and M. Chatterjee (1994). Local scour due to submerged horizontal jet. *Journal of Hydraulic Engineering 120*(8), 973–992.

Chou, Y.-J. and O. B. Fringer (2010). A model for the simulation of coupled flow-bed form evolution in turbulent flows. *Journal of Geophysical Research: Oceans (1978–2012) 115*(C10).

Cundall, P. A. and O. D. Strack (1979). A discrete numerical model for granular assemblies. *Geotechnique 29*(1), 47–65.

Deen, N., M. Van Sint Annaland, M. Van der Hoef, and J. Kuipers (2007). Review of discrete particle modeling of fluidized beds. *Chemical Engineering Science 62*(1), 28–44.

Desjardins, O., G. Blanquart, G. Balarac, and H. Pitsch (2008). High order conservative finite difference scheme for variable density low mach number turbulent flows. *Journal of Computational Physics 227*(15), 7125–7159.

Doligalski, T., C. Smith, and J. Walker (1994). Vortex interactions with walls. *Annual Review of Fluid Mechanics 26*(1), 573–616.

Frank, E. and F. Jørgen (1976). A sediment transport model for straight alluvial channels. *Nordic Hydrology 7*(5), 293–306.

Hamidifar, H., M. Omid, and M. Nasrabadi (2011). Scour downstream of a rough rigid apron. *World Applied Sciences Journal 14*(8), 1169–1178.

Hoffmans, G. and H. Verheij (1997). *Scour manual*. Balkema Rotterdam, The Netherlands.

Hoffmans, G. J. (2012). *The influence of turbulence on soil erosion*, Volume 10. Eburon Uitgeverij BV.

Hogg, A. J., H. E. Huppert, and W. B. Dade (1997). Erosion by planar turbulent wall jets. *Journal of Fluid Mechanics 338*, 317–340.

Hopfinger, E., A. Kurniawan, W. Graf, U. Lemmin, et al. (2004). Sediment erosion by görtler vortices: the scour-hole problem. *Journal of Fluid Mechanics 520*, 327–342.

IPCC (2007). Climate change 2007: Synthesis report. contribution of working groups i, ii and iii to the fourth assessment report of the Intergovernmental Panel on climate change. Technical report, IPCC, Geneva, Switzerland. Core Writing Team, Pachauri, R.K and Reisinger, A. (eds.).

Kidanemariam, A. G. and M. Uhlmann (2014). Direct numerical simulation of pattern formation in subaqueous sediment. *Journal of Fluid Mechanics 750*, R2.

BIBLIOGRAPHY

Kramer, W., H. Clercx, and G. van Heijst (2007). Vorticity dynamics of a dipole colliding with a no-slip wall. *Physics of Fluids (1994-present) 19*(12), 126603.

Kravchenko, A. G., C. HAECHEON, and P. Moin (1993). On the relation of near-wall streamwise vortices to wall skin friction in turbulent boundary layers. *Physics of fluids. A, Fluid dynamics 5*(12), 3307–3309.

Lagasse, P., J. Schall, F. Johnson, E. Richardson, and F. Change (1995). Stream stability at highway structures. Technical Report Report Num. FHWA-HI-96-032, Federal Highway Administration.

Li, F. and L. Cheng (1999). Numerical model for local scour under offshore pipelines. *Journal of Hydraulic Engineering 125*(4), 400–406.

Liang, D., L. Cheng, and F. Li (2005). Numerical modeling of flow and scour below a pipeline in currents: Part ii. scour simulation. *Coastal engineering 52*(1), 43–62.

Lim, J., H. Choi, and J. Kim (1998). Control of streamwise vortices with uniform magnetic fluxes. *Physics of Fluids (1994-present) 10*(8), 1997–2005.

Liu, X. and M. H. García (2008). Three-dimensional numerical model with free water surface and mesh deformation for local sediment scour. *Journal of waterway, port, coastal, and ocean engineering 134*(4), 203–217.

Masuda, N., J. Yoshida, B. Ito, T. Furuya, and O. Sano (2012). Collision of a vortex ring on granular material. part i. interaction of the vortex ring with the granular layer. *Fluid Dynamics Research 44*(1), 015501.

Melville, B. W. and S. E. Coleman (2000). *Bridge scour*. Water Resources Publication.

Meyer-Peter, E. and R. Müller (1948). Formulas for bed-load transport. In *Proceedings of the 2nd Meeting of the International Association for Hydraulic Structures Research*, pp. 39–64. Stockholm.

Munro, R., N. Bethke, and S. Dalziel (2009). Sediment resuspension and erosion by vortex rings. *Physics of Fluids 21*, 046601.

Mutlu Sumer, B. (2007). Mathematical modelling of scour: A review. *Journal of Hydraulic Research 45*(6), 723–735.

Nik Hassan, N. and R. Narayanan (1985). Local scour downstream of an apron. *Journal of Hydraulic Engineering 111*(11), 1371–1384.

Olsen, N. R. and H. M. Kjellesvig (1998). Three-dimensional numerical flow modeling for estimation of maximum local scour depth. *Journal of Hydraulic Research 36*(4), 579–590.

Olsen, N. R. and M. C. Melaaen (1993). Three-dimensional calculation of scour around cylinders. *Journal of Hydraulic Engineering 119*(9), 1048–1054.

Paola, C. and V. Voller (2005). A generalized exner equation for sediment mass balance. *Journal of Geophysical Research: Earth Surface (2003–2012) 110*(F4).

Pealer, S. (2012). Lessons from Irene: Building resiliency as we rebuild. Technical report, Vermont Agency of Natural Resources.

Pepiot, P. and O. Desjardins (2012). Numerical analysis of the dynamics of two-and three-dimensional fluidized bed reactors using an euler–lagrange approach. *Powder Technology 220*, 104–121.

Roulund, A., B. M. Sumer, J. Fredsøe, and J. Michelsen (2005). Numerical and experimental investigation of flow and scour around a circular pile. *Journal of Fluid Mechanics 534*, 351–401.

Sano, O., T. Furuya, and B. Ito (2008). Collision of a vortex ring on granular layer. In *IUTAM Symposium 150 Years of Vortex Dynamics (October 2008)*.

Tao, J. and X. Yu (2013). A framework for numerical simulation of bridge scour focusing on the improvements of sediment transport models. In *Transportation Research Board 92nd Annual Meeting*, Number 13-2852.

USGCRP (2009). Global climate change impacts in the Unites States. Technical report, U.S. Global Change Research Program.

Uyumaz, A. (1988). Scour downstream of vertical gate. *Journal of Hydraulic Engineering 114*(7), 811–816.

Van Rijn, L. C. (1984). Sediment transport, part i: bed load transport. *Journal of hydraulic engineering 110*(10), 1431–1456.

van Rijn, L. C. (1987). *Mathematical modelling of morphological processes in the case of suspended sediment transport*. Ph. D. thesis, Waterloopkundig Lab., Delft Hydraulics Comm-382.

von Helmholtz, H. (1867). On integrals of the hydrodynamical equations, which express vortex-motion. *Philosophical Magazine Series 4 (18511875) 33*. 1867 translation of 1858 journal article.

Wardhana, K. and F. C. Hadipriono (2003). Analysis of recent bridge failures in the United States. *Journal of Performance of Constructed Facilities 17*(3), 144–150.

Yoshida, J., N. Masuda, B. Ito, T. Furuya, and O. Sano (2012). Collision of a vortex ring on granular material. part ii. erosion of the granular layer. *Fluid Dynamics Research 44*(1), 015502.

Zamankhan, P. (2009). Analysis of submarine pipeline scour using large-eddy simulation of dense particle-liquid flows. *Journal of offshore mechanics and Arctic engineering 131*(2).

Zhu, H., Z. Zhou, R. Yang, and A. Yu (2007). Discrete particle simulation of particulate systems: theoretical developments. *Chemical Engineering Science 62*(13), 3378–3396.

Zhu, H., Z. Zhou, R. Yang, and A. Yu (2008). Discrete particle simulation of particulate systems: A review of major applications and findings. *Chemical Engineering Science 63*(23), 5728–5770.

Chapter 3

Future Work

This work is the foundation for a large amount of possible future projects. Three-dimensional simulations hold the potential for significant advancement of knowledge about fundamental scour mechanisms. Possible future work includes reproducing the experimental work of Munro (Munro et al. 2009) and Sano et al. (Sano et al. 2008), who generated 3D vortex rings which impinged a particle bed. A logical extension of this work would be to place strong stream wise vortices (represented by cylindrically extended vortex dipoles) into a turbulent channel, or boundary layer, flow. Kidanemariam and Uhlmann (Kidanemariam and Uhlmann 2014) have simulated channel flow over a particle bed to analyze pattern formation in the bed. The coupling between such a flow and the particle bed are not well understood, so a further study into the effects of the entrained particles on the turbulent structures of the flow, and the mechanisms of the pattern formation, or scour, would be a contribution.

Our group also hopes to improve considerably on our particle model by linking Large-scale Atomic/Molecular Massively Parallel Simulator (LAMMPS), a molecular dynamics (MD) code, to Arts, the code we use in collaboration with Olivier Desjardin's group at Cornell University. LAMMPS is a widely used state-of-the-art MD code maintained by Sandia National Laboratories, that includes an exhaustive library of molecules and their relevant properties. Ideally, the particle-particle and particle-wall collisions would be handles by LAMMPS, and Arts would integrate the flow variables. The method used in this work is limited to spherical (circular in 2D) particles, but if LAMMPS were linked to Arts, the sediment particles could take

on any shape or configuration that is found in the LAMMPS libraries. This sort of multiscale modeling is still very new and would be a great contribution.

Bibliography

Barbhuiya, A. K. and S. Dey (2004). Local scour at abutments: A review. In *Sadhana: Academy Proceedings in Engineering Sciences*, Volume 29, pp. 449–476. Indian Academy of Sciences.

Beetstra, R., M. Van der Hoef, and J. Kuipers (2007). Drag force of intermediate reynolds number flow past mono-and bidisperse arrays of spheres. *AIChE Journal 53*(2), 489–501.

Betts, A. (2011). Climate change in Vermont. Technical report, Vermont Agency of Natural Resources. Climate Change Adaption White Paper Series.

Bove, I., D. Acosta, N. Gutiérreza, V. Gutiérreza, and L. Sarasúa (2013). Double scouring by turbulent jets downstream of a submerged sluice gate. *arXiv preprint arXiv:1311.4194*.

Breusers, H. and A. J. Raudkivi (1991). *Scouring*. AA Balkema Rotterdam,, The Netherlands.

Brørs, B. (1999). Numerical modeling of flow and scour at pipelines. *Journal of Hydraulic Engineering 125*(5), 511–523.

Chatterjee, S., S. Ghosh, and M. Chatterjee (1994). Local scour due to submerged horizontal jet. *Journal of Hydraulic Engineering 120*(8), 973–992.

Chou, Y.-J. and O. B. Fringer (2010). A model for the simulation of coupled flow-bed form evolution in turbulent flows. *Journal of Geophysical Research: Oceans (1978–2012) 115*(C10).

Cundall, P. A. and O. D. Strack (1979). A discrete numerical model for granular assemblies. *Geotechnique 29*(1), 47–65.

Deen, N., M. Van Sint Annaland, M. Van der Hoef, and J. Kuipers (2007). Review of discrete particle modeling of fluidized beds. *Chemical Engineering Science 62*(1), 28–44.

Desjardins, O., G. Blanquart, G. Balarac, and H. Pitsch (2008). High order conservative finite difference scheme for variable density low mach number turbulent flows. *Journal of Computational Physics 227*(15), 7125–7159.

Doligalski, T., C. Smith, and J. Walker (1994). Vortex interactions with walls. *Annual Review of Fluid Mechanics 26*(1), 573–616.

Frank, E. and F. Jørgen (1976). A sediment transport model for straight alluvial channels. *Nordic Hydrology 7*(5), 293–306.

Hamidifar, H., M. Omid, and M. Nasrabadi (2011). Scour downstream of a rough rigid apron. *World Applied Sciences Journal 14*(8), 1169–1178.

Hoffmans, G. and H. Verheij (1997). *Scour manual*. Balkema Rotterdam, The Netherlands.

Hoffmans, G. J. (2012). *The influence of turbulence on soil erosion*, Volume 10. Eburon Uitgeverij BV.

Hogg, A. J., H. E. Huppert, and W. B. Dade (1997). Erosion by planar turbulent wall jets. *Journal of Fluid Mechanics 338*, 317–340.

Hopfinger, E., A. Kurniawan, W. Graf, U. Lemmin, et al. (2004). Sediment erosion by görtler vortices: the scour-hole problem. *Journal of Fluid Mechanics 520*, 327–342.

IPCC (2007). Climate change 2007: Synthesis report. contribution of working groups i, ii and iii to the fourth assessment report of the Intergovernmental Panel on climate change. Technical report, IPCC, Geneva, Switzerland. Core Writing Team, Pachauri, R.K and Reisinger, A. (eds.).

Kidanemariam, A. G. and M. Uhlmann (2014). Direct numerical simulation of pattern formation in subaqueous sediment. *Journal of Fluid Mechanics 750*, R2.

Kramer, W., H. Clercx, and G. van Heijst (2007). Vorticity dynamics of a dipole colliding with a no-slip wall. *Physics of Fluids (1994-present) 19*(12), 126603.

Kravchenko, A. G., C. HAECHEON, and P. Moin (1993). On the relation of near-wall streamwise vortices to wall skin friction in turbulent boundary layers. *Physics of fluids. A, Fluid dynamics 5*(12), 3307–3309.

Lagasse, P., J. Schall, F. Johnson, E. Richardson, and F. Change (1995). Stream stability at highway structures. Technical Report Report Num. FHWA-HI-96-032, Federal Highway Administration.

Li, F. and L. Cheng (1999). Numerical model for local scour under offshore pipelines. *Journal of Hydraulic Engineering 125*(4), 400–406.

Liang, D., L. Cheng, and F. Li (2005). Numerical modeling of flow and scour below a pipeline in currents: Part ii. scour simulation. *Coastal engineering 52*(1), 43–62.

Lim, J., H. Choi, and J. Kim (1998). Control of streamwise vortices with uniform magnetic fluxes. *Physics of Fluids (1994-present) 10*(8), 1997–2005.

Liu, X. and M. H. García (2008). Three-dimensional numerical model with free water surface and mesh deformation for local sediment scour. *Journal of waterway, port, coastal, and ocean engineering 134*(4), 203–217.

Masuda, N., J. Yoshida, B. Ito, T. Furuya, and O. Sano (2012). Collision of a vortex ring on granular material. part i. interaction of the vortex ring with the granular layer. *Fluid Dynamics Research 44*(1), 015501.

Melville, B. W. and S. E. Coleman (2000). *Bridge scour*. Water Resources Publication.

Meyer-Peter, E. and R. Müller (1948). Formulas for bed-load transport. In *Proceedings of the 2nd Meeting of the International Association for Hydraulic Structures Research*, pp. 39–64. Stockholm.

Munro, R., N. Bethke, and S. Dalziel (2009). Sediment resuspension and erosion by vortex rings. *Physics of Fluids 21*, 046601.

Mutlu Sumer, B. (2007). Mathematical modelling of scour: A review. *Journal of Hydraulic Research 45*(6), 723–735.

Nik Hassan, N. and R. Narayanan (1985). Local scour downstream of an apron. *Journal of Hydraulic Engineering 111*(11), 1371–1384.

Olsen, N. R. and H. M. Kjellesvig (1998). Three-dimensional numerical flow modeling for estimation of maximum local scour depth. *Journal of Hydraulic Research 36*(4), 579–590.

Olsen, N. R. and M. C. Melaaen (1993). Three-dimensional calculation of scour around cylinders. *Journal of Hydraulic Engineering 119*(9), 1048–1054.

Paola, C. and V. Voller (2005). A generalized exner equation for sediment mass balance. *Journal of Geophysical Research: Earth Surface (2003–2012) 110*(F4).

Pealer, S. (2012). Lessons from Irene: Building resiliency as we rebuild. Technical report, Vermont Agency of Natural Resources.

Pepiot, P. and O. Desjardins (2012). Numerical analysis of the dynamics of two-and three-dimensional fluidized bed reactors using an euler–lagrange approach. *Powder Technology 220*, 104–121.

Roulund, A., B. M. Sumer, J. Fredsøe, and J. Michelsen (2005). Numerical and experimental investigation of flow and scour around a circular pile. *Journal of Fluid Mechanics 534*, 351–401.

Sano, O., T. Furuya, and B. Ito (2008). Collision of a vortex ring on granular layer. In *IUTAM Symposium 150 Years of Vortex Dynamics (October 2008)*.

Tao, J. and X. Yu (2013). A framework for numerical simulation of bridge scour focusing on the improvements of sediment transport models. In *Transportation Research Board 92nd Annual Meeting*, Number 13-2852.

USGCRP (2009). Global climate change impacts in the Unites States. Technical report, U.S. Global Change Research Program.

Uyumaz, A. (1988). Scour downstream of vertical gate. *Journal of Hydraulic Engineering 114*(7), 811–816.

Van Rijn, L. C. (1984). Sediment transport, part i: bed load transport. *Journal of hydraulic engineering 110*(10), 1431–1456.

van Rijn, L. C. (1987). *Mathematical modelling of morphological processes in the case of suspended sediment transport*. Ph. D. thesis, Waterloopkundig Lab., Delft Hydraulics Comm-382.

von Helmholtz, H. (1867). On integrals of the hydrodynamical equations, which express vortex-motion. *Philosophical Magazine Series 4 (18511875) 33*. 1867 translation of 1858 journal article.

Wardhana, K. and F. C. Hadipriono (2003). Analysis of recent bridge failures in the United States. *Journal of Performance of Constructed Facilities 17*(3), 144–150.

Yoshida, J., N. Masuda, B. Ito, T. Furuya, and O. Sano (2012). Collision of a vortex ring on granular material. part ii. erosion of the granular layer. *Fluid Dynamics Research 44*(1), 015502.

Zamankhan, P. (2009). Analysis of submarine pipeline scour using large-eddy simulation of dense particle-liquid flows. *Journal of offshore mechanics and Arctic engineering 131*(2).

Zhu, H., Z. Zhou, R. Yang, and A. Yu (2007). Discrete particle simulation of particulate systems: theoretical developments. *Chemical Engineering Science 62*(13), 3378–3396.

Zhu, H., Z. Zhou, R. Yang, and A. Yu (2008). Discrete particle simulation of particulate systems: A review of major applications and findings. *Chemical Engineering Science 63*(23), 5728–5770.